Energetic Materials Frontiers 4 (2023) 140–157

Contents lists available at ScienceDirect

Energetic Materials Frontiers

journal homepage: www.keaipublishing.com/en/journals/energetic-materials-frontiers

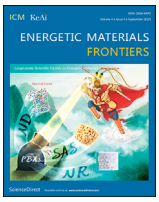

A review of small angle scattering, neutron reflection, and neutron diffraction techniques for microstructural characterization of polymer-bonded explosives

Liang-fei Bai [a], Xin-xi Li [a], Hao Li [a], Guang-ai Sun [a,*], Dong Liu [a], Zhan-yu wu [a], Mei Peng [a], Zhi-chao Zhu [a], Chao-qiang Huang [a], Fei-yan Gong [b], Shi-chun Li [b]

[a] Key Laboratory of Neutron Physics and Institute of Nuclear Physics and Chemistry INPC, China Academy of Engineering Physics CAEP, Mianyang, 621999, China
[b] Institute of Chemical Materials, China Academy of Engineering Physics CAEP, Mianyang, 621999, China

ARTICLE INFO

Keywords:
Small-angle scattering
Neutron reflection
Neutron diffraction
Microstructures
Void structure
Interfacial structure

ABSTRACT

To better understand the structure-activity relationship and enhance the overall performance of polymer-bonded explosives (PBXs), the neutron and X-ray scattering techniques, which utilize neutron or X-ray radiation as probes, are unique and useful methods for quantifying the inherent hierarchical microstructures and components of PBXs. This review focuses on a series of scattering techniques and their typical applications in PBXs and includes a brief introduction of large neutron and X-ray scientific facilities in China. It describes the basic principles, instrumentation, sample environment, and empirical approaches of small-angle scattering (SAS), neutron reflection (NR), and neutron diffraction (ND). Additionally, it reviews common applications of these scattering techniques in the fields of PBXs. Combining the scattering techniques with complementary methods yields several valuable parameters that account for the microstructural features of PBXs. The combination can be used to establish multi-scale structure-activity relationships of PBXs and optimize the preparation process, numerical simulations, and performance prediction of PBXs. More efforts should be made to (1) gather the comprehensive multi-scale microstructural parameters for certain PBXs and add them to corresponding characteristic databases; (2) further investigate the dependence of the microstructural features on the preparation conditions of PBXs; (3) establish multi-factor correlations between the multi-scale microstructural features and the multiple performances obtained from experiments; (4) incorporate the microstructural parameters into various theoretical computational models.

1. Introduction

Polymer-bonded explosives (PBXs), primarily consisting of highly explosive powder bound with a small quantity of polymer binders and additives,[1] are significant energetic materials with outstanding performances due to their well-balanced mechanical properties, processing and manipulations, and detonation behavior. Usually, PBXs are subjected to severe temperature, pressure, and mechanical conditions during their manufacture.[2] For example, PBX 9501,[3] PBX 9502,[4] LX 17[5], other HMX-based PBXs,[6] and TATB-based PBXs[7] experience temperatures of greater than 100 °C and pressure of approximately 100–200 MPa. The complex fabrication procedures and heterogeneous components cause PBX materials to possess various microstructures, including voids or pores, cracks, material interfaces, and micro-strains, which have a size range of more than six orders of magnitude from several angstroms to hundreds of microns. Moreover, such microstructures gradually evolve when being insulted by thermal, stress, vibration, or chemical conditions during machining, storing, transportation, and serving. Extensive experimental studies have revealed that the multi-scale microstructures of PBXs can affect their macroscopic properties, such as shock sensitivity,[8,9] flame propagation,[10] detonation,[11] mechanical deformation,[12] mechanical strength,[4] and thermal stability.[6,13] These effects are still ambiguous partly due to the difficulty in qualifying the sophisticated microstructures of PBXs.[14] Therefore, qualifying the microstructural features of PBXs is essential for establishing the quantitative relationship between their structures and properties.[14,15]

Over the past three decades, various microscopy and tomography techniques have been used to reveal the external and partial internal

* Corresponding author.
E-mail address: guangaisun_80@163.com (G.-a. Sun).

https://doi.org/10.1016/j.enmf.2023.01.001
Received 26 August 2022; Received in revised form 5 November 2022; Accepted 20 January 2023
Available online 23 January 2023

microstructural characteristics of PBXs. For example, optical microscopy is one of the earliest techniques used to observe the external morphology of PBX 9501.[16–20] This technique can semi-quantitatively yield the size, shape, and distribution of the damage to explosive crystals, cracks, or binders, spanning sizes from several microns to hundreds of microns. The combination of a polarized light optical microscope (PLOM) and the refractive index matching method[8,21] can further reveal information about the internal defects or voids embedded in explosive crystals. A scanning electron microscope (SEM) is another useful tool for characterizing the external morphology and certain inner characteristics of PBXs, with resolutions ranging from tens of nanometers to hundreds of microns,[22–24] but using it requires a broken or polished specimen. Atomic force microscopy (AFM)[12,25] and transmission electron microscope[26–28] (TEM) are occasionally used to provide surface morphology and interfacial structures of PBXs with higher resolutions. To reconstruct a three-dimensional (3D) structure, X-ray computed microtomography[29–31] (XRCT) and nano-CT[32,33] have recently been used to obtain spatial distribution information on the voids, cracks, explosive crystals, and binders within PBXs. These techniques can directly image with an adjustable resolution. However, the non-bulk statistical characteristics and the destructive sample preparations make them less convenient and satisfactory in obtaining deep information on specimens.

Furthermore, fluid-invasion methods, namely gaseous adsorption[34,35] (BET) and mercury intrusion porosimetry[36–38] (MIP), are occasionally applied to measure the porosity, particle size, and specific surface area of PBXs. Both methods can only catch open pores. The BET is a good choice for nanopores, while the MIP may destroy the pore structure due to the high pressure and brittle-plasticity characteristics of PBXs. In addition, X-ray photoelectron spectroscopy[39,40] (XPS) and Infrared Spectroscopy[41] (IR) are sometimes utilized to infer the interfacial structure by comparing the changes in certain atomic bonding. However, these methods provide only qualitative information and are limited to specific systems.

The neutron and X-ray scattering techniques, such as small-angle X-ray scattering (SAXS),[16] ultra-small angle X-ray scattering (USAXS),[42] small-angle neutron scattering (SANS),[43] ultra-small angle neutron scattering (USANS),[9] NR,[12] and ND,[44] are powerful tools for characterizing the microstructures of PBXs. For SAS, neutrons or X-ray beams are incident on the bulk PBX specimens and are scattered near the initial direction,[45] providing information on the size distribution of voids, specific interfacial area, and fractal structures.[46] For NR, neutrons are reflected by the surfaces and interfaces of modeled PBX thin films,[12] providing information on the thickness, roughness, and consisting of interfacial microcosmic structures. For ND, scattered neutrons satisfying the Bragg condition can provide information on crystal structure and microstrains.[47,48] Scattering techniques enjoy the following advantages.[49] First, they provide high-quality statistical and quantitative structural information, which facilitates the direct comparison among different samples. Second, due to the penetrating ability of X-rays and especially neutrons, diverse apparatuses can be utilized to control environmental conditions, such as cryostat, heating oven, compressing equipment, stretcher, and cell for controlling atmospheric conditions. This advantage facilitates the performance of in-situ experiments and the investigation of corresponding microstructural evolution progresses. Third, an appropriate combination of SAXS, USAXS, SANS, and USANS allows for determining the features of voids, binders, and interfaces on a scale of sub-nanometer to roughly 20 mm (0.5 nm–20 μm), which are crucial to material characterization.[15,50,51] Fourth, the contrast variation by replacing some components yields partial scattering information,[18,51] which is useful for distinguishing different types of interfaces or voids of explosive crystals and binders. Owing to these advantages, scattering techniques have been widely used to characterize various PBX materials. The demand for investigating PBXs and their components using scattering techniques has increased recently due to the rapid development of large neutron and X-ray scientific facilities in China.

Herein, this review summarized some typical applications to promote research on PBXs using scattering techniques. This review consists of the followings parts: (1) a brief introduction of available large neutron and X-ray scientific facilities in China; (2) an overview of the principles of SAS, NR, and ND for characterizing PBXs, including the description of the experimental process, apparatuses used to control the in-situ environment conditions, and some typical sample conditions and fitting models for PBXs; (3) an overview of the typical applications of SAS, NR, and ND for characterizing PBXs, (4) and a discussion of the complementary methods and prospect of some promising subjects for the development and application of scattering techniques.

2. Overview of large X-ray and neutron scientific facilities in China

Over the past decades, dozens of light sources and neutron sources have been constructed in the world, and their detailed information can be found on websites such as lightsources.org and neutronsources.org,.[52,53] China has devoted numerous human and financial resources to the construction of science facilities and has made remarkable achievements. Synchrotron radiation facilities, such as the Beijing Synchrotron Radiation Facility (BSRF),[54,55] the National Synchrotron Radiation Lab (NSRL, Hefei),[56,57] and the Shanghai Synchrotron Radiation Facility (SSRF),[58–62] have played an important role in scientific investigations. As a typical third-generation SR facility, the SSRF can provide hard X-ray beams and makes it easy to perform scattering experiments with a spatial resolution of ~100 nm or a time resolution of sub-ms level.[61]

China has constructed three neutron scattering facilities for scattering research, namely, the China Spallation Neutron Source (CSNS),[63–67] the China Advanced Research Reactor (CARR),[63,68] and the China Mianyang Research Reactor (CMRR).[69–71] The CSNS is a multidisciplinary user facility that can accelerate proton beam pulses to 1.6 GeV kinetic energy with a 25 Hz repetition rate to produce spallation neutrons under a beam power of 140 kW. The CSNS was officially open to users from 2018 and contains SANS,[64] NR,[67] GPND,[66] Multi-Physics Instrument (MPI),[72] and the latest VSANS instruments.[73] The CMRR is a 20 MW nuclear reactor with a liquid hydrogen cold neutron source, which owns eight neutron instruments currently in operation (i.e., HRND,[74] RSND,[75] HPND,[76] TNR, CTAS,[71] SANS,[77] TPNR,[78] and CNR[79]) and eight instruments under construction, including spin-echo SANS,[80] USANS[70] and so on.

China has more than 10 available instruments based on large X-ray and neutron facilities for characterizing PBXs currently. Regarding SAS instruments based on larger X-ray facilities, there are three operating SAXS instruments (e.g., the BSRF 1W2A beamline,[55] SSRF BL16B1 beamline,[59] and SSRF BL19U2 beamline[60]) and one USAXS instrument at SSRF BL10U1.[62] There are two operating SANS instruments, namely Suanni at CMRR[81] and SANS at CSNS.[64] Moreover, tools in commission at CMRR include the Bixi USANS with a maximal detectable size of 20 μm and the spin-echo small-angle neutron scattering with a maximal detectable size of 10 μm, and a very small angle neutron scattering at CSNS is under construction.[70,80] Two NR instruments are currently online, namely the Diting at CMRR[78] and a multipurpose neutron reflectometer at CSNS.[67] Four instruments are available for ND, namely the Xuanwu at CMRR,[74] the Fenghuang at CMRR,[76] the general purpose powder diffractometer at CSNS, and the multi-physics instrument at CSNS.[66] Detailed information on these instruments can be found in available literature, and their capabilities to characterize the typical microstructures of PBXs are illustrated in Fig. 1. As large neutron and X-ray scientific facilities have rapidly developed in China and especially the CMRR equipped with SANS, USANS,NR, and ND instruments runs 200 days a year, more opportunities are offered to the energetic material community.

3. Overview of several neutron and X-ray scattering techniques

3.1. SAS

SAS is a highly elastic scattering phenomenon wherein light, X-ray, or

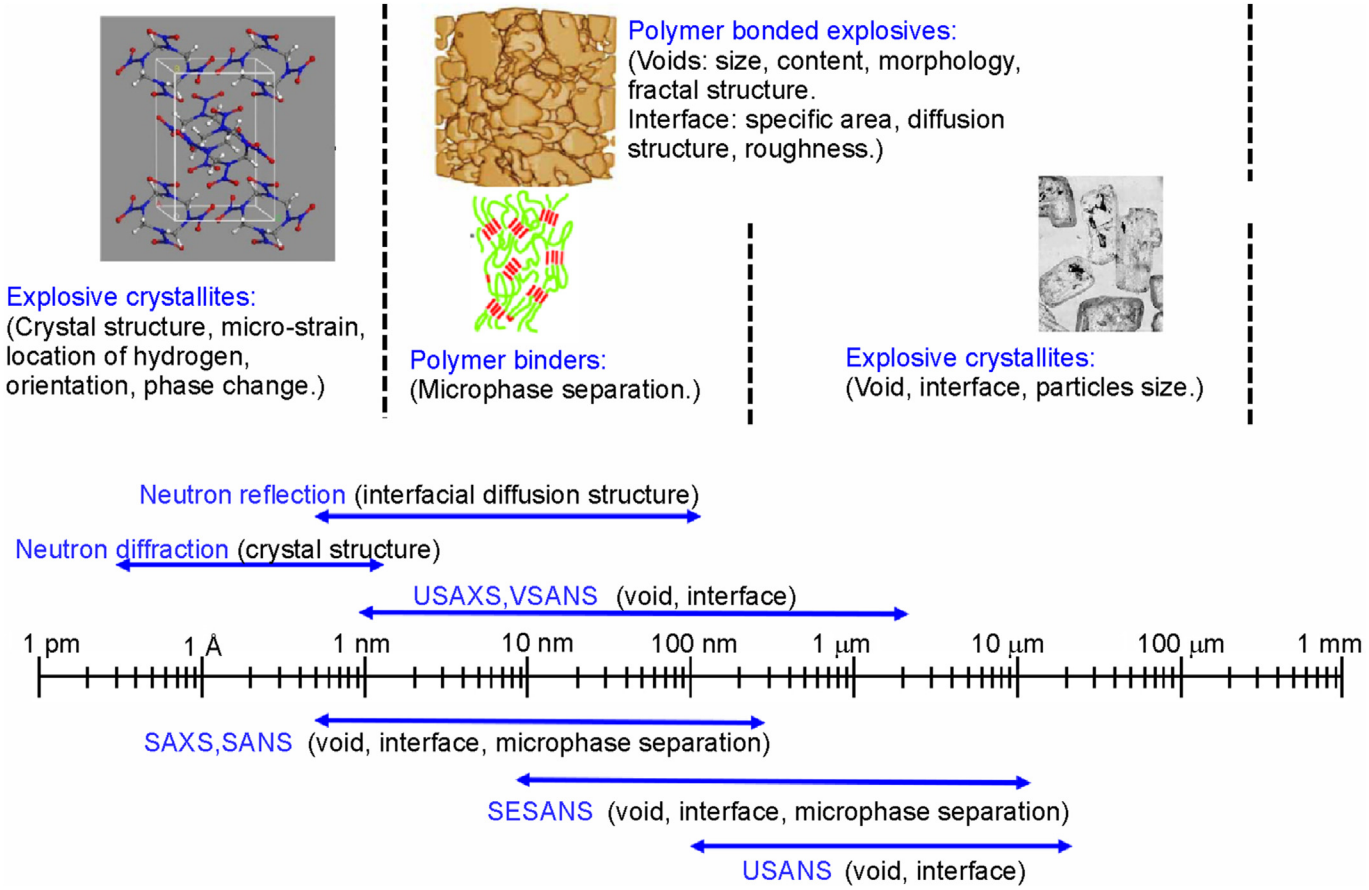

Fig. 1. Typical microstructures of PBXs and the corresponding size ranges characterized using SAS, NR, and ND.

neutron radiation diverges from their incident beam by a small scattering angle,[82] 2θ, as it penetrates through a sample. Generally, the scattering angle of SAS is less than 10°, and diverged scattering arises from the inhomogeneous microstructures (called scatterers) on a length scale of several nanometers to tens of microns, which translates into neutron scattering length density (SLD) or electron density, $\rho(r)$. In PBXs, the inhomogeneous microstructures include voids, porosity, cracks, interfaces, explosive crystals, and binders.

To simplify the analysis procedure of SAS, the scattering angle, 2θ, and the radiation wavelength, λ, are usually encoded to one scattering wavevector, Q, which is defined as $Q = 4\pi\sin\theta/\lambda$. The SAS experiment process then measures the Q dependence of the radiation scattering intensity, I(Q), as a function of Q. According to the SAS theory,[82] when the radiation is only scattered once by the sample, I(Q) is proportional to the squared Fourier transform of neutron SLD or electron density, $\rho(r)$. Therefore, important parameters that indicate statistical features of the scatterers within the sample can be quantified by fitting the I(Q) curves with various models. For PBXs, these statistical parameters can be attributed to voids (the size distribution, morphology, fractal structures, and the content of internal or external voids from 1 nm to 20 μm),[9,42,50] interfaces (specific interfacial area and fractal dimension),[7,51] binders (the size distribution and morphologies of fillings),[50] and explosive crystals (particle size, morphology, and specific surface area).[83] For more in-depth information about the instrumental configurations, general experimental processes, and data processing procedures of SAS, the book by Hamley is recommended.[82] This review focuses on the special requirements for sample conditions, available sample environment, and some of the commonly used fitting models for PBXs.

In standard SAS experiments, including SAXS, USXNS, SANS, and USANS, a variety of specimens with different forms can be used, including explosive crystallite powders, PBX modeling powders, and compactions of explosive crystallites or PBX composites. Using a contrast variation method, all of the aforementioned specimens can be immerged in solutions with a special container (e.g., quartz cell for neutrons and plastic capillary for X-ray). Generally, the beam sizes for X-ray SAS instruments are less than 1 mm × 1 mm[61], and that for neutrons are on the order of magnitude of 1 cm × 1 cm. Therefore, the area of the tested samples should be larger than the beam sizes. Moreover, the thickness of the tested sample should be around 1 mm, as a thick sample can lead to multiple scattering and a thin sample can lead to weak signals.[84]

Benefiting from the advantage of high flux (X-ray beams) or deep penetration (neutron beams), many environmental instruments are equipped with various SAS instruments for in-situ experiments.[5,43,85–87] Temperature control apparatuses and mechanical loading devices are frequently used to investigate the microstructural evolution of PBX materials, and selected devices are listed in Table 1. Moreover, Tian et al. (2019)[88] reviewed several apparatuses equipped for the Suanni SANS instrument at CMRR, including a miniature oven for temperature control

Table 1
Selected temperature apparatus for in-situ SAS experiments of PBXs.

Apparatus	In-situ experiment	SAS instruments	Reference
Temperature cycling apparatus	−55 °C and 70 °C, TATB-based PBXs	USAXS at 32-ID APS	Trevor et al. (2009)[5]
Modified THMS600	25 °C and 200 °C, HMX-based PBXs	USAXS at 15-ID-D	Trevor et al. (2015)[85]
THMS600 stage	25 °C and 200 °C, HMX-based PBXs	SAXS at BL16B1 SSRF	Yan et al. (2016)[43]
Small tubular heater	25 °C and 185 °C, HMX-based PBXs	SANS at Suanni CMRR	Yan et al. (2017)[86]
TCS 300 stage	25 °C and 185 °C, HMX	SAXSpace	Shi et al. (2020)[87]

and two types of mechanical apparatuses (a miniature mechanical testing machine and a compressing loading device) for mechanical loading. Recently, a new hot stage with seven individual channels has been developed at CMRR. This instrument can accomplish thermal cycling from RT to 250 °C for seven PBX samples, respectively, using an individual temperature controller, which is extremely convenient for auto-batch testing (Fig. 2).

To interpret the SAS results of PBXs, the first step is to analyze the primary sources of SAS[42,50] by comparing the SLD (Table 2) between the components of tested systems.[5,8,9,37,43,50,89] The difference in the SLD ($\Delta\rho$, contrast) is usually small for the explosive crystallites and binders among most composite PBX materials. In this case, the void scattering predominates and a two-phase assumption (void and matrix phases, including explosive crystallites and binders) is usually adopted. The remarkable difference in neutron SLD between the normal and perdeuterated binder for PBX9501, cyclohexane, and methanol enables the contrast variation method to be used in SANS experiments, where primary scattering sources should be particularly considered and a two-phase or three-phase assumption can be applied.[50]

As mentioned above, parameters indicating the statistical features of the microstructures of PBX materials are extracted by fitting the *I(Q)* curves with different models. Because the obtained *I(Q)* curves from specific SAS instruments contain no phase information and have limited *Q* ranges, there may be more than one physical model fitting a given *I(Q)* curve well. Several useful approaches have been frequently used to interpret the *I(Q)* curves of PBXs based on the two-phase or three-phase assumption.

The first approach is the power law and the Porod analysis.[17] In the case of a high *Q* range, the scattering curves can usually be described using the power law, $I(Q) = C_0 + C_4 * Q^{-\alpha}$, where α, C_4, and C_0 are constants. α of 0–3 reflects a mass fractal dimension, and α of 3–4 reflects a rough interface with a surface fractal dimension of 6-α. α of 4 indicates Porod scattering. In this case, $C_4 = 2\pi S(\Delta\rho)$,[2] where *S* is the specific surface area and $\Delta\rho$ is the contrast. The Porod analysis can be used to determine whether the interfaces between the scatterers and the surrounding media are smooth and not fractal and provide the exact values of various specific interface areas.

The second approach is the calculation of the scattering invariant (Φ).[8] Normally, a sufficiently large *Q* range is required to accurately calculate the scattering invariant. However, it is impossible to get enough low *Q* for PBXs in real SAS experiments, and thus the pseudo-invariants from the measured *Q* range are commonly used. For a pure two-phase system, the pseudo-invariant (Φ) can be described using the following equation:

Table 2
List of SLD for some standard components in tested PBX systems (the values maybe slightly different in different literature).

Component	X-ray SLD (× 10^{10} cm^{-2})	Neutron SLD (× 10^{10} cm^{-2})	Reference
TATB	~16.4	~4.87	Trevor et al. (2009)[5]
Kel-F 800	~15	~3.98	Joseph et al. (2020)[90]
HMX	~16.7	~4.50	Joseph et al. (2010)[50]
F2314	~16.5	~3.95	Yan et al. (2016)[43]
Binder for PBX9501	~14.8	~1.99	Joseph et al. (2010)[50]
Deuterated binder for PBX9501	~14.8	~3.22	Joseph et al. (2010)[50]
RDX	~15.9	~4.34	Chad et al. (2010)[8]
Cyclohexane	~7.5	~-0.28	Joseph et al. (2000)[37]
Deuterated cyclohexane	~7.5	~6.68	Joseph et al. (2000)[37]
Methanol	~7.56	~-3.73	Song et al. (2019)[89]
Deuterated methanol	~7.56	~5.80	Song et al. (2019)[89]
Void	0	0	–

$$\Phi = \int_{Q1}^{Q2} Q^2 I^{'}(Q)\mathrm{d}Q = 2\pi^2(\Delta\rho)^2\varphi(1-\varphi) \quad (1)$$

where $I^{'}(Q)$ is the scattering intensity with background subtracted, cm^{-1}, *Q* is the scattering wavevector, $Å^{-1}$, $\Delta\rho$ is the SLD contrast, cm^{-2}, and φ is the volume fraction of scatters, dimensionless. The void volume fraction in PBXs can be estimated.

The third approach is to fit the SAS curves using the size distribution models associated with highly polydisperse, uncorrelated dilute particles.[37,42,43,50] Given that voids are the minority phase for most of the composite PBX materials or explosive crystallites, the dilute particles with uncorrelated positions and random orientations are frequently assumed, and $I^{'}(Q)$ can be written as:

$$I^{'}(Q) = (\Delta\rho)^2 \int_0^{\infty} NP(D)V^2(D)F^2(Q,D)\mathrm{d}D \quad (2)$$

where *D* is the particle diameter, Å; $F^2(Q, D)$ is the form factor; $V(D)$ is the particle volume, $Å^3$; *N* is the total number of particles per unit volume, dimensionless, and $P(D)$ is the probability of particles with size *D*, dimensionless. To get the size distribution of voids, their geometric form

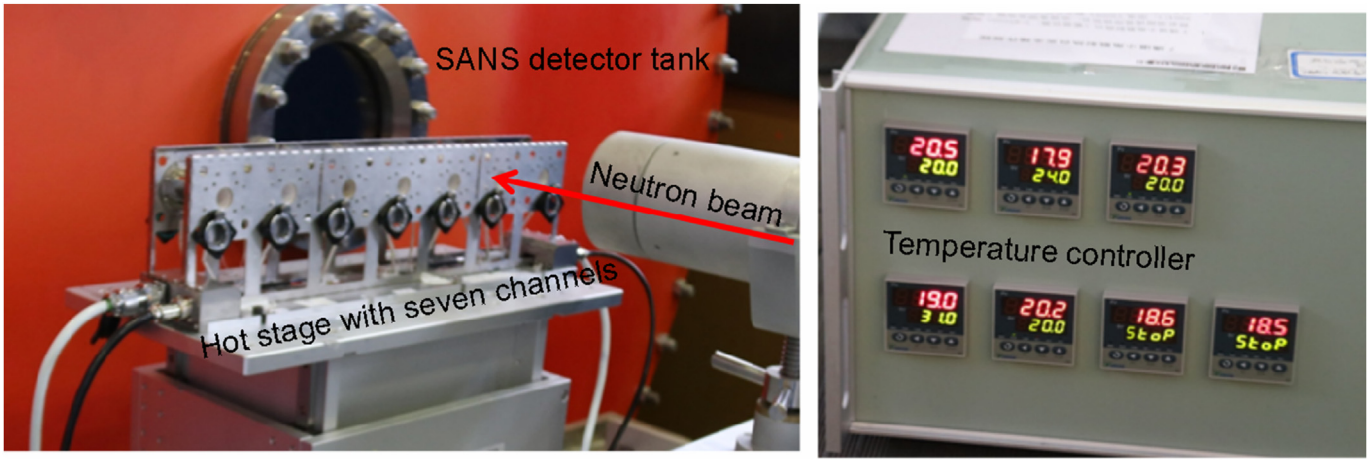

Fig. 2. Hot stage with seven individual channels for in-situ SAS experiments of PBX materials.

can be assumed to be a spherical[42] (commonly used) or a non-spherical morphology[50] (e.g., cylindrical) and can then be extracted by assuming special distribution functions (e.g., Lognormal probability distribution function)[37] or using the maximum entropy algorithm.[86]

Recently, some fractal models with the assumption of correlated ramified void structures have been used for PBX materials.[8,9,89,91] Joseph et al. (2013)[91] extracted the surface-defined mean size and volume fractal dimensions of voids using a sophisticated model. Song et al. (2019)[89] described the voids with a two-level volume fractal structure using the Beaucage model. Joseph et al. (2020)[90] extracted the radius of gyration of the void correlation distance, the void radius of gyration, and the volume and surface dimensions of the voids using a modified Ornstein-Zernike (MOZ) model. However, the model that can best describe real structures of voids and interfaces within PBXs is still debatable and further investigation is required.

3.2. NR

NR is a powerful tool for studying the surfaces and interfaces of thin films in biology and materials science.[3,12,92,93] Specular neutron reflectivity provides information on SLD profiles perpendicular to the sample surface, and thus the characteristics of layers, such as thickness, surface roughness, interfacial roughness, composition, and defects can be measured with a high spatial resolution on a nanometric scale. The essence of a specular NR experiment is to obtain the neutron reflectivity as a function of the scattering vector, Q_z, which is perpendicular to the sample surface. In addition to specular neutron reflectivity, the off-specular neutron reflectivity probes the lateral correlations of interfacial roughness and artificial large-scale lateral structures.

During a NR experiment, a neutron beam illuminates a PBX sample at a very low angle (2θ), and the reflectivity (R)—the ratio of the intensity of the incident beam to the reflected beam—is measured using a neutron detector. Moreover, the time-of-flight method is used to determine the wavelength of the neutrons, (λ), and the reflectivity is measured as a function of the magnitude of the momentum transfer vector $Q_z = 4\pi\sin(\theta)/\lambda$ based on several incident angles. By modeling the reflectivity curve, the real-space SLD, which is a function of both the density and the chemical composition of the materials, can be obtained normally to the interface of the thin film. To this end, the established model of the reflectivity curve is composed of discrete layers of homogeneous materials characterized by parameters including the thickness, SLD, and interfacial roughness of the sample, and the associated scattering signals are calculated. The genetic and least-square fitting algorithms are commonly used to minimize the differences between the model and the actual data. For a heterogeneous film, the SLD can be estimated to be a function of the depth in a sample assuming that lateral variation in the sample is minimal.

Neutrons are sensitive to light elements,[49] which are the main components of PBXs, explosive crystals, and binders. Compared with other detection methods, NR can accurately characterize the surface and interface microstructures of thin films. On the contrary, X-ray reflection is not sensitive to light elements and can only reflect the microstructure of some binders, and it is difficult to obtain the accurate thickness of some explosive crystals, such as HMX thin films. Other commonly used interface characterization tools, such as ellipsometry and atomic force microscope, are usually fast and convenient and are more suitable for simple film structures,[94] though it is difficult to obtain precise microstructural parameters of complex film structures.

To mimic the progress in the PBX preparation process, samples are commonly prepared by sequential dip-coating of HMX and binders from solutions onto silicon substrates to create a layered interface structure. The HMX-binder interface is formed by coating the completely dry polycrystalline HMX surface using the bulk formulation solvent for polymer binders.

There is a time-of-flight mode neutron reflectometer Diting[78] at CMRR, and it has been in service for nearly 10 years. Various sample environmental devices are available, such as environment simulation devices of temperature and humidity, dip coating machines, spin coating machines, high-precision microscopes, and aging simulation equipment.

Neutrons have a large penetration depth and are non-destructive, making it easy to perform in-situ experiments and learn the interfaces of explosives and binders. The crystal-binder interface directly affects the PBX stability, interfacial bond strength, aging cracking, and phase transition temperature. Many studies have been conducted on the crystal-binder interface using the NR technique.[12,93–95]

3.3. ND

ND is a standard technique for accurately determining the crystal structure on an atomic scale. The key principle of ND is the Bragg equation[96]:

$$n\lambda = 2d\sin\theta \tag{3}$$

where λ is the wavelength, Å; n is the coefficient of wavelength; d is the interfacial distance, Å, and 2θ is the diffraction angle, degree. Reflection occurs when the Bragg equation is met. A diffractometer is designed to quantify λ and θ simultaneously and ubiquitously to determine the lattice spacing, d. Lattice structures can then be deduced theoretically using some crystallographic procedures.

However, data analysis is complicated in practice due to apparatus statuses, experimental operations, and sample structure uncertainties such as variations in lattice parameters and atomic coordinates, thermal vibrations, and other possible structural changes induced by preprocessing or environmental conditions. For powder diffraction, the overlapping of reflection caused by similar or equal d values can also lead to considerable information loss. Thereby, a rational process of diffraction data should consider the above items as far as possible. The Rietveld method can deal with the overlapping of reflection, as the structural parameters can be obtained from powder patterns with intensities at individual Bragg reflection instead of integrated intensities.[97,98] The key is the shape of the diffraction peak, for which the pseudo-Voigt function is commonly used in neutron powder diffraction.[99] Well-established software, such as Fullprof and GSAS, is available to deal with complicated situations.[100,101]

It is noteworthy that the hydrogen in energetic materials contributes considerable incoherent scattering, which results in high background noise and consequently reduces the signal-noise ratio. If this is unacceptable, a conventional way to solve the problem is to predestinate samples.[102,103] Samples for ND should be well crystallized. Owing to the size effect, the domain size (which is different from the particle size, unless the sample is a single crystal) should be controlled at an order of magnitude of 10^{-1}–10^{2} μm. Typical ND studies concerning energetic materials involve thermodynamic transition, which requires in-situ environmental conditions, such as thermal or high-pressure treatments. Two diffractometers at CMRR, namely Fenghuang and Xuanwu, are equipped with numerous in-situ environmental apparatuses with a maximum pressure load of 2000 kN and a temperature range of 4–1873 K.[74,76,104] After rational sample preprocessing, experimental operation, and data analysis, sufficient information can be obtained from ND to study the structural evolution such as constitutions, phase transitions, and microstrains on an atomic scale.

4. Recent applications in the characterization of PBXs

4.1. Multi-scale microstructures derived from SAS

SAS has been widely used to characterize the microstructures of PBXs and their evolution under stimulated environmental conditions on a length scale of 1 nm–20 μm. This section reviews the typical applications of six rough categories of PBX composites and their main components and explosive crystallites according to certain common features of

samples or microstructures. The applications of binders can be found in other literature.[88]

4.1.1. Porosity and surface characteristics of explosive crystallite powders

PBXs usually have high content of explosive crystallites as the major power source. For example, PBX 9501 has octogen (HMX) content of 95%,[17] the PBXN series have hexogen (RDX) content of greater than 60%,[105] and LX 17 and PBX 9502 have 1,3,5-Triamino-2,4,6-trinitrobenzene (TATB) content of 92.5%[42] and 95%,[42] respectively. Though some initial structures of the explosive crystallite powders could be altered during the complicated manufacturing processes of PBXs, their comprehensive characterization is still significant for establishing some intrinsic relationships. The most concerned structural factors for explosive crystallite powders include particle size distribution, polymorph, morphology, surface area, and microstructure, which could be associated with the overall performance of explosive crystallite powders. With the advantages of convenient statistic making, a simple testing process, and available contrast variation, SAS is widely utilized to measure a series of microstructural parameters of explosive crystallite powders, including specific surface area, fractal behavior, pore-size distribution, and particle size. This study roughly classified these applications into two situations according to whether the contrast variation method is used or not.

Benefiting from the quite different coherent neutron scattering cross-sections of hydrogen and deuterium, it is relatively easy to find an appropriate deuterated/nondeuterated solution to match the neutron SLD of explosive crystallites through SANS experiments. Moreover, the explosive crystallites should be insoluble and sufficiently infiltrated in fluids. Therefore, the contrast variation SANS (CV-SANS) has long been used.

In 2000, Joseph et al. (2000)[37] first conducted CV-SANS experiments on HMX crystallite powders to gauge the different effects of mechanical deformation on coarse and fine HMX particles. They observed that all HMX particles had smooth external surfaces (on the length scale of SANS measurement, R: 1.0–60 nm). As shown by the Porod analysis, coarse HMX particles had a specific surface area of 0.28 $m^2\ g^{-1}$, which increased to 0.65 $m^2\ g^{-1}$ after compression, while fine HMX particles had a specific surface area of 3.61 $m^2\ g^{-1}$, which decreased to 2.64 $m^2\ g^{-1}$ after compression. These changing trends were similar to the results of Hg porosimetry. They proposed that the mechanical deformation of the coarse HMX particles was dominated by the breaking and cracking of crystallites, while that of the fine HMX particles included the collapse of cracks and the compression of crystallites.[37] Moreover, the models used to fit the Gaussian distributions of polydisperse spherical voids provided the internal pore size distribution. The coarse HMX particles showed one single broad distribution (centered on $R = 25.0$ nm), and the compression divided them into two distinct populations (centered on $R = 3.3$ nm and 28.7 nm). By contrast, the fine HMX particles consisted of two distinct void populations (centered on $R = 2.9$ nm and 15.5 nm), and the compression greatly reduced the peak area of the large voids and reduced small dimensions (centered on $R = 1.6$ nm). They considered that the compression squeezed out large voids and induced ramified cracking. Joseph et al. (2000)[83] performed similar CV-SANS experiments on four types of loose TATB powders, yielding similar results that the mean size of the internal voids decreased with the grinding. Therefore, CV-SANS is an effective tool to characterize the internal porosity and external surface structure of explosive powders.

Considering the limited measurement range of Q of SANS, Chad et al. (2010)[8] first combined SANS with USANS to investigate the discrepant features of internal voids in five types of RDX crystallites with similar densities and particle size distributions produced by four manufacturers. Contrast-matched SAS measurement revealed that the dominant feature of all samples was surface fractal behavior with a fractal dimension of 2.4–2.9 on a length scale of 50 nm–20 μm. The surface fractal behavior arose from the crystal growth, and the most significant differences among the samples were the pseudo-invariants calculated in a Q range of ($3 \times 10^{-5} - 10^{-2}$) $Å^{-1}$. They were well consistent with the shock sensitivity obtained from large-scale gap tests. The above study was also the first try to establish a direct link between microstructural scattering parameters and the tested results of shock sensitivity.

Later, Song et al. (2019)[89] measured the fractal behavior and porosity of micro/nano-sized TATB crystallites using a similar CV-SANS method. They observed that micro-sized TATB crystallites had smooth external surfaces while nano-sized TATB crystallites exhibited a surface fractal structure (surface fractal dimension: $2.36 < D_S < 2.55$). For internal pores, micro- and nano-sized TATB crystallites exhibited a surface fractal structure (surface fractal dimension: $2.15 < Ds < 2.25$) and a two-level volume fractal structure, respectively. This study was the first try to describe the pore structures of energetic materials using the Beaucage model.

It is generally difficult to implement contrast variation SAXS (CV-SAXS) for explosive crystallites. In 2013, Mark et al.[106] used a 60% $ZnBr_2/H_2O$ solution to match the x-ray scattering contrast of TATB and identify the internal closed porosity. They conducted a series of USAXS experiments to evaluate the microstructural differences between new and legacy dry aminated TATB powders. They observed that all the dry TATB powders showed the same morphology on a length scale of nanometers to microns and that the approximate intra-crystalline voids contributed to the overall LX-17 porosity distribution. Moreover, they found that the incomplete filling of the intercrystalline areas and various hydrophobicity might affect the extraction reliability of the internal porosity of TATB powders.

Recently, another series of perfluoropolyethers (PFPEs) with different molecular weights have been used for CV-SAXS. In 2020, Wang et al. (2020)[107] first demonstrated the feasibility of CV-SAXS experiments using GPL-107 PFPE on HMX and 2,4,6,8,10,12-hexanitrohexaazaisowurtzitane (CL-20) crystallites. They determined the volume fraction and specific surface of the internal voids in three types of CL-20 crystallites with different mean sizes, which decreased with an increase in the crystal size. This result was consistent with the density measured using a particle density distribution analyzer (PDDA). Later, using the same method, Yu et al. (2021)[108] demonstrated that numerous voids or cracks arose inside the 2,6-diamino-3,5-dinitropyrazine-1-oxide (LLM-105) crystals during the preheating.

Xing et al. (2022)[109] also conducted CV-SAXS experiments on three sizes of micro/nano LLM-105 crystallites using GPL-105 PFPE. They observed that all the surfaces exhibited a surface fractal structure and that the surface fractal dimension increased with the particle size but the void volume decreased with the particle size in the measurement range of Q. Besides, using the maximum entropy fitting method, they found that the increased amplitude of the void volume was greater when the particle size decreased from 3 μm to 500 nm than that when the particle size decreased from 500 nm to 200 nm.

There are lots of other applications of the SAS experiments on explosive crystallite powders without using the contrast variation method. In such cases, the scattering information from the external surface, inter-space between particles, and internal voids could not be distinguished, and several interpretations have been reported to obtain different types of features.

The first interpretation assumes that the scattering signals mainly originate from explosive particles. In 2000, Joseph et al. (2000)[83] obtained the average particle sizes of several types of loose powders through USAXS measurement, with the obtained average particle sizes agreeing well with the results obtained using a laser diffraction analyzer (LDA).

The second interpretation assumes that the scattering signals primarily originate from pores, including open and closed pores. In 2003, Chen et al. (2003)[110] found that the mean pore sizes of three kinds of TATB powders increased with an increase in the particle size through SAXS. Similarly, Xia et al. (2005)[111] obtained the mean size, specific surface area, surface fractal dimension, interface thickness, and radius of gyration of the pores in seven types of TATB loose powders, which would be affected by the preparation conditions. In 2020, Shi et al. (2020)[87]

performed in-situ SAXS experiments on two types of HMX crystallites under temperatures of 30–200 °C. They first observed that the defects with a radius of gyration of about 0.6–0.9 nm appeared in both samples when being heated above 150 °C and that larger crystallites had higher defect volume ratios. Combining the results of WAXS and scanning electron microscopy, they proposed that smaller HMX crystallites (5 μm) had higher thermal stability.

The third interpretation assumes that the scattering signals primarily originate from internal voids. In 2010, Yan et al. (2010)[112] performed SAXS experiments on four types of RDX crystallites. They found that all the radii of gyration of pores approximated 42 nm, all the mean void radii from Gaussian distributions that were assumed to have a spherical morphology were nearly 63 nm, and the interface area of internal pores decreased with an increase in the particle size. In 2011, Tian et al. (2011)[113] obtained the internal void distribution of three types of CL-20 from SAXS. They proposed that the CL-20 prepared using the evaporation method exhibited the highest crystal quality compared with raw materials and CL-20 obtained using the sedimentation method. In 2013, Tian et al. (2013)[114] studied the microstructural variations of CL-20 crystallites induced by thermal treatment through SAXS experiments. They found that the interface area and the void volume increased by 5.4- and 5.2-fold, respectively after the phase transition at 170 °C and that a large number of voids would be produced both in bulk and on surface due to thermal decomposition after heating at 200 °C for 5 h.

4.1.2. Microstructures of compactions of explosive crystallites

Because of the simple composition, compactions of explosive crystallites are another type of samples concerned. Their microstructures could be measured using the SAS techniques to help fully understand the sophisticated microstructures or some mechanical properties of PBXs.

In 2000, Joseph et al. (2000)[84] first conducted USAXS experiments on four pressed dry aminated TATB (DA-TATB) pellets with different thicknesses and a similar density of 1.60 g cm^{-3}. They observed that the USAXS curves of the samples with thicknesses of 0.05 cm and 0.1 cm exhibited the same shape, with the first knee indicating a pore radius of 2.8 μm, while those of the samples with thicknesses of 0.2 cm and 0.3 cm showed severe multiple scattering, with the first knee indicating a pseudo pore radius of 2.4 μm. Later, Trevor et al. (2006)[42] conducted USAXS experiments on consolidated ultra-fine TATB. They found that the samples showed a smooth material-void interface and the void size distribution contained two overlapping peaks, with the second peak located near 35 nm and the void volume having a total measured fraction of 3.6%.

In 2008, Mark et al. (2008)[115] conducted USAXS experiments on TATB disks to evaluate the different interfacial characteristics of TATB powders. Despite the occurrence of multiple scattering, the qualitative analysis still revealed that the power-law exponent of the ATK TATB was −3.42, indicating a diffuse or rough fractal surface and that the power-law exponents of wet-aminated TATB (−3.89–3.94), dry-aminated TATB (−3.85–3.90), and even the Holsten (−3.97) were immediately close to −4, indicating a smooth interface between TATB and air.

In 2013, Joseph et al. (2013)[91] conducted USANS and SANS experiments on pressed TATB pellets to study the fractal networks of intergranular voids. They processed the USANS curves using a sophisticated model including both fractal and isolated voids. They discovered that the intergranular voids of loose powders were randomly arranged with a surface-defined mean size of 0.66 μm but those of pressed samples showed a fractal network with rough interfaces. Both the surface-defined mean size and the volume fractal dimension of the voids in the pressed samples first increased and then decreased with an increase in the pressed density (up to 1.720 g cm^{-3}), as shown in Fig. 3a. Based on these transitions, Joseph et al. proposed that TATB particles exhibited brittle behavior at low pressed density and ductile behavior at high pressed density. Joseph et al. (2013)[116] conducted a similar study of pressed diaminoazoxyfurazan (DAAF) pellets. They found that the mean void sizes ranged from 0.059 μm to 0.195 μm and decreased monotonically with an increase in the applied density for all three types of DAAF pellets but that the volume fractal dimensions ranged from 2.13 to 2.78 and increased with an increase in the applied density. Furthermore, both the volume fractal dimension and the mean void size appeared to converge to a common value among the three different DAAF systems, which were obviously different from the TATB system, as shown in Fig. 3b.

4.1.3. Interfacial surface structures of PBXs

There are three types of interfaces in pressed PBX composites, namely explosive crystal-binder, explosive crystal-void, and binder-void interfaces. These interfaces concern extensively as they may influence the integrated mechanical performance and the detonation performance of PBX composites by affecting the transmission properties of micro-stresses and the hot spot formation under shock conditions. Since the Porod analysis and the power law can provide information on the interfaces,

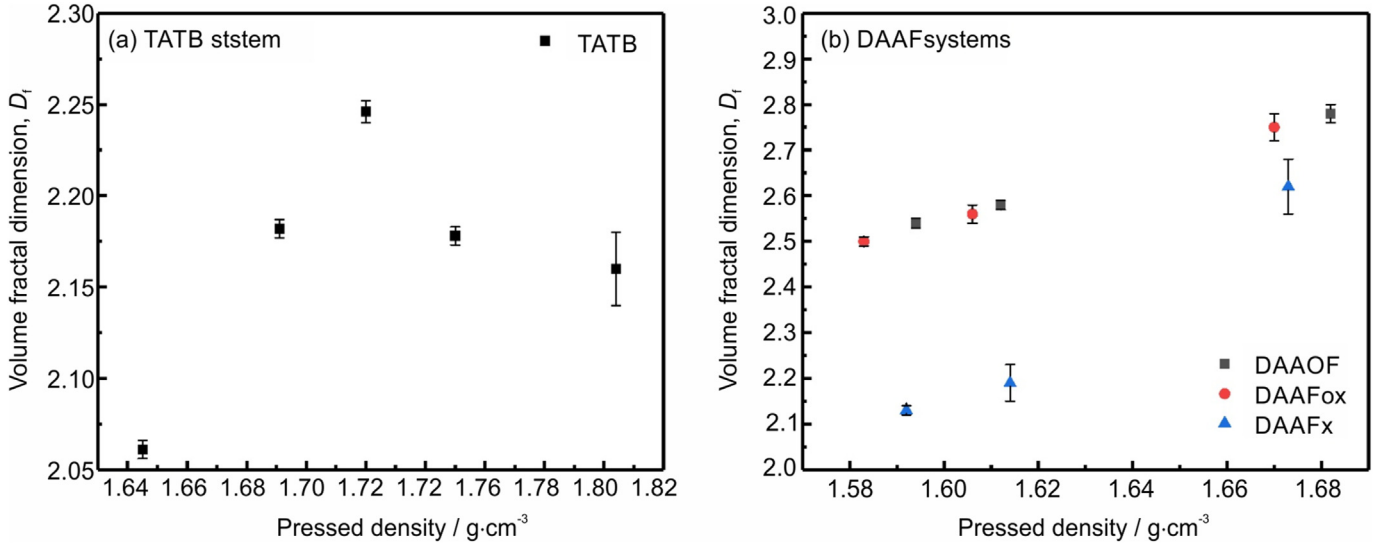

Fig. 3. Dependence of the void volume fractal dimension on the pressed density. (a) TATB system (increasing up to a density of 1.720 g cm^{-3} and decreasing thereafter),[91] and (b) three types of DAAF powders with different mean particle sizes prepared through different synthesis routes (volume fractal dimensions increasing monotonically with the pressed densities and appearing to converge to a common value).[116]

this section focuses on the applications of SAS techniques in providing specific surface area and surface fractal dimension of the above interfaces, aiming to help material scientists deeply understand the pressing mechanisms or enhanced mechanical properties of PBXs.

The CV-SANS can distinguish scattering signals from different interfaces and thus has long been used to quantify the three types of interface areas in PBX materials. To conduct CV-SANS experiments, two methods have been developed to vary the neutron SLD of tested samples. At least three levels of different contrasts could be accomplished to facilitate solving the three-parameter equations of different interfaces.

One method is to use a mixture of perdeuterated/nondeuterated solutions to infiltrate the PBX samples. In 2006, Joseph et al. (2006)[117] conducted CV-SANS experiments on PBX 9501 samples swollen by toluene. Although the interfaces might be slightly perturbed by the swelling process, the SANS data analysis can still yield the pressure-dependent three types of surface areas, namely HMX-binder (S_{HB}), HMX-void (S_{HV}), and binder-void (S_{BV}).

Another method is to use a mixture of perdeuterated/nondeuterated binders. In 2011, Joseph et al. (2011)[51] conducted CV-SANS experiments on PBX 9501 and obtained the dependence of interface areas on hot-pressing pressure of 69–200 MPa, as shown in Fig. 4a. According to this figure, the area of the HMX-binder interface increased with an increase in the pressure, while the area of the HMX-void interface decreased slightly. Joseph et al. (2011)[51] proposed that the net increase in the total interface area should be attributed to the brittle fractures of HMX crystals. In 2019, Bai et al. (2019)[18] conducted CV-SANS experiments on HMX-based PBXs and obtained the dependence of interface areas on cold-pressing pressure of 64–382 MPa, as shown in Fig. 4b. Based on the SANS results, they first proposed the concept of interfacial binding rate between HMX and binders, which was the ratio of S_{HB} to the sum of S_{HB} and S_{HV}. It was observed that the interfacial binding rate between HMX and binders increased greatly in the pressure range, revealing that a large quantity of binders were extruded and in contact with the surface of HMX crystals. Bai et al. (2019)[18] also found that the sum of S_{HB} and S_{HV} changed little during the cold pressing and demonstrated that a small quantity of HMX crystals occurred in the transgranular fractures under the as-implemented condition. This finding was quite different from the hot-pressing process of PBX 9501.

Besides the above contrast variation methods, Trevino (2008)[118] developed a novel method of SANS combined with SAXS in 2008. This method is used to achieve sufficient contrast variation for a partial solution of the three-parameter equation to evaluate mechanically induced damage. SAS experiments were performed on four PBX composites, namely PBX 9404, PBX 9501, PBX 9502, and PAX 2A, before and after deformation under different cylindrical axial strains. The Porod analysis showed that the filler particles in all four materials had no preferred alignment and the binder efficiently coated the filler particles. Moreover, only the filler-binder specific surface area of the most severely deformed samples increased relatively largely due to the fractures of filler particles and coverage with the binder.

Normal SAS experiments were widely used to determine the interfacial structures of PBXs under the two-phase assumption. Peterson et al. (2005)[17] conducted MSAXS experiments on PBX 9501 samples in 2005. After thermal treatment using three different temperature regimes, they obtained the temperature dependence of the total surface area, reflecting the thermally induced cracks and pores. Moreover, the interface fractal dimensions could also be extracted. In 2020, He et al. (2020)[7] conducted SANS experiments on TATB-based PBX composites to measure the fractal dimensions of interfaces. The SANS results implied that the PBX composites based on TATB particles with a core-shell-shell structure had much rough interfaces, which would help enhance the interfacial interactions.

4.1.4. Porosity and microstructures of HMX-based PBXs

Porosity is considered one of the most important microstructural parameters of PBX materials. According to the hot-spot models, the voids of 100 nm to 1 μm in PBXs influence the initiation and detonation properties of PBXs. With the advantage of appropriate detectable scales, SAS techniques, especially USAXS and USANS, are widely utilized to measure the porosity of PBXs due to different motivations for evaluating the thermally or mechanically induced damage, exploring the void evolution mechanism, optimizing the formulations, and providing basic void data for the theoretical mode. Similar to those applications for measuring interface characteristics, most SAS experiments were conducted directly using the PBX samples without contrast variation. Moreover, two-phase models composed of voids and bulk matrix were used to interpret the SAS data, assuming that the voids were the primary scattering source.

The HMX-based PBX materials show relatively complex microstructural evolution induced by thermal treatment due to multiple physical changes including thermal expansion, crystalline phase change, binder melting and filling, and Ostwald ripening. SAS techniques have been extensively used to quantify the process and reveal the mechanism over the past twenty years.

In 2002, Joseph et al. (2002)[16] conducted USAXS experiments on

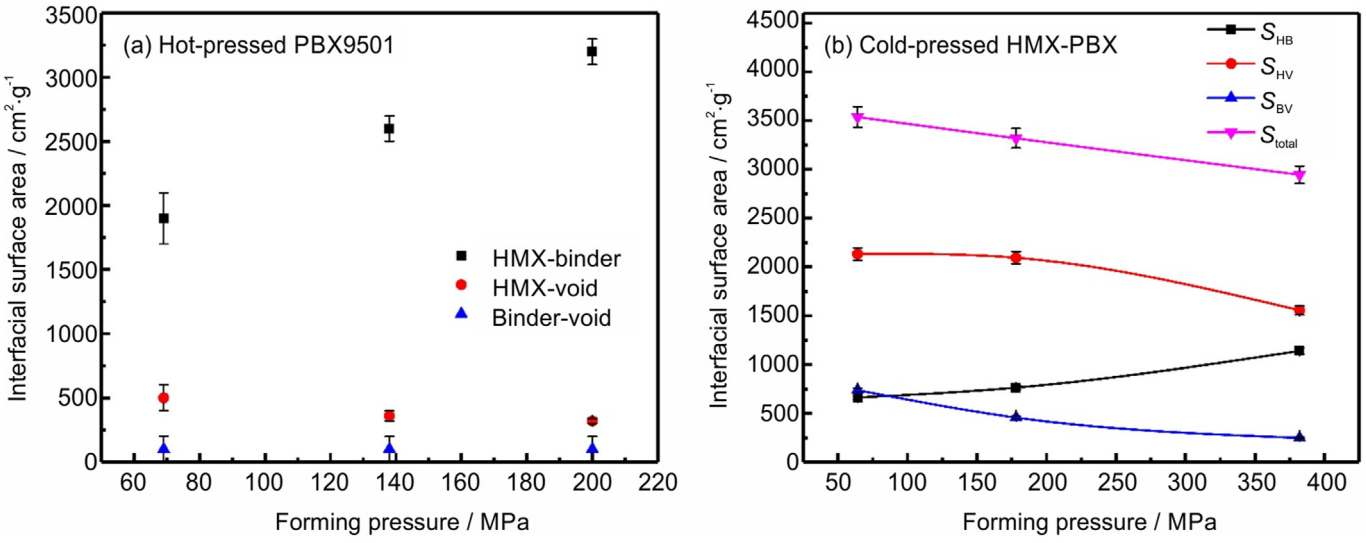

Fig. 4. Changes in various types of interface areas extracted from the SANS results of the PBXs under the forming pressure (S_{total} is the sum of the three types of interface areas, S_{HB} is the area of the HMX-binder interface, and S_{BV} is the area of the binder-void interface). (a) Hot-pressed PBX 9501,[51] (b) cold-pressed HMX-based PBX.[18]

pristine PBX 9501 and obtained a trimodal distribution of pores using a model of Gaussian distributions and spherical pores. In 2005, Peterson et al. (2005)[17] conducted similar experiments on PBX 9501 samples to quantify the thermal damage through thermal treatment. The sample treated at the lowest temperature of 159 °C showed a single pore distribution (centered on R = 260 nm). The second population of small pores (centered on R = 10.7 nm) appeared at a temperature of above 176 °C, with the size increased to 21.0 nm at 190 °C. Peterson et al. (2005)[17] proposed that the thermal damage to PBX 9501 was dominated by crystalline phase change, thermal expansion, and Ostwald ripening at low-temperature regimes (155–174 °C) and by chemical decomposition at high-temperature regimes (175–210 °C). In 2014, Yan et al. (2014)[119] conducted SAXS experiments on two types of HMX-based PBXs with different HMX mean particle sizes after being thermally treated at three different temperatures in the air. They found that great changes in the two types of samples occurred at 180 °C and 200 °C, which resulted from phase transformation and exothermic decomposition, respectively.

In 2015, Trevor et al. (2015)[85] conducted in-situ USAXS experiments on LX 10 and PBX 9501 under temperatures of 25–200 °C. They found that the mesoscale structures of LX 10 and PBX 9501 were relatively stable until 175 °C and both samples showed broad size distributions. However, dramatic changes occurred promptly with the phase transition of β-δ rather than with other thermal effects, forming a bimodal distribution. They also found that the mesoscale structure of LX-10 did not change so severely as that of PBX 9501 during cooling but failed to give a satisfactory explanation (partially because they ignored the difference in the HMX phase structure after cooling to room temperature).

In 2016, Yan et al. (2016)[43] conducted in-situ SANS and SAXS experiments on HMX-based PBXs. The Porod analysis indicated that the interface area decreased dramatically by 60% during the heating from 100 °C to 200 °C. This result suggested that the filling of initial voids with melted F2314 was predominant due to the relatively low density of HMX-based PBXs used in the study (compared with LX 10 and PBX 9501). Surprisingly, the void volume distribution of the thermally treated HMX-based PBXs showed that voids with sizes of 15–35 nm increased greatly during the storage at RT in the first 3 h. Sooner, Yan et al. (2017)[86] conducted further in-situ SANS experiments on thermally treated HMX-based PBXs in dry and humid atmospheres, respectively. They obtained the dependence of the void volume fraction on the storage time and demonstrated that the relative humidity of 60% extensively accelerated the increase of the void volume fraction, which was caused by the phase retransformation from δ-HMX to β-HMX.

In addition, there are two reports stating that the contrast variation method was used to probe the porosity of HMX-based PBXs. In 2000, Joseph et al. (2000)[37] first tried to conduct contrast-matched SANS experiments on a PBX 9501 sample using a deuterated solution. They found two distinct signals on the SANS curve, which might arise from the internal voids and the polymer binder, respectively. In 2009, Joseph et al. (2009)[5] conducted CV-USANS experiments on PBX 9501 using a mixed deuterated binder (Estane and plasticizer) to measure the porosity on a length scale of 0.1–20 μm under applied pressure of 69–200 MPa. The volume fractions of HMX, binders, and voids in the PBX 9501 were determined through the Porod invariant analysis and structural modeling. They were consistent with the pressed density estimates and showed no significant difference under different pressures. The spherical modeling provided the dependence of the void and binder size distributions on the hot-pressing intensity, suggesting that the binders would spread out and fill some of the small voids at high applied pressures.

4.1.5. Porosity and microstructures of TATB-based PBXs

Owing to the remarkable anisotropic thermal properties and sheet-like molecule structure of TATB, TATB-based PBX materials exhibit intriguing microstructures and irreversible volumetric thermal expansion called ratchet growth. SAS techniques have been frequently used to investigate the significant alteration in void size distribution and the mechanisms associated with ratchet growth.

To investigate the effects of thermal cycling on void size distribution, Trevor et al. (2006)[42] conducted USAXS experiments on LX 17–1 and PBX 9502 samples in 2006, both of which were processed and subjected to thermal cycling. The USAXS data were fitted using a model of spheres and the maximum entropy algorithm. Both the pristine LX 17–1 and PBX 9502 exhibited a bimodal distribution with a narrow peak around 7–10 nm and a broad peak over 20 nm–1 μm. After 12 thermal cycles under temperatures of 74–54 °C, both the number and size of the large voids significantly increased. Trevor et al. (2006)[42] proposed that small voids should be attributed to the intrinsic porosity of TATB crystallites but large voids should result from intercrystalline areas as a result of consolidation. In 2009, Trevor et al. (2009)[120] further combined USAXS, USANS, and X-ray computed tomography (on a focused ion beam instrument, XRCT, FIB) for LX 17 samples before and after temperature cycling, as shown in Fig. 5. The void sizes from a few nanometers to about 15 μm were obtained by interpreting the results using the three techniques based on certain similar assumptions and were plotted on the same axes. The combination of the three techniques provided important data and a comprehensive characterization method for completely understanding the structure of PBXs from nanometers to centimeters, which could be useful for designing next-generation TATB-based PBXs.

To deduce the ratchet growth mechanism, Trevor et al. (2009)[5] conducted in-situ USAXS experiments on different formulations of LX 17, UFTATB, and three other PBXs under thermal cycling at a temperature of -55–70 °C in 2009. The TATB-based PBX samples were determined to have void sizes of about 2 nm to 2 μm. After 2.5 cycles, two samples containing Cytop M (0.9%–1.3%) and Cytop A (0.6%–1.1%) showed a small increase in volume while the sample containing Hyflon (1.6%–4.6%) showed a large increase in volume compared with LX 17 (1.4%–3.5%). Moreover, Trevor et al. (2009)[5] found that the void structure of LX 17 mainly changed during the heating portion of the cycling and above the glass transition temperature of the binders. In conjunction with mesoscale modeling, they proposed that high glass transition temperature, high adhesion of TATB binder, and wetting were all crucial to minimizing the ratchet growth of TATB-based PBXs.

To investigate the effects of ratchet growth, Thompson et al. (2010)[4] conducted USANS experiments on PBX 9502 before and after thermal cycling at a temperature of -55–80 °C in 2010. As revealed by the void volume under a size range of 0.1–10 μm extracted from the USANS results, samples with ratchet growth contained more numerous and smaller voids than the newly pressed sample with the same density. This result suggested that the pore structures of thermally damaged materials may be more contiguous and connected, which will account for the lower tensile and compressive moduli.

To accurately measure the void morphology, Joseph et al. (2020)[90] conducted SANS and USANS experiments on two PBX 9502 samples uniaxially pressed in directions parallel and perpendicular to the compaction plane in 2020, respectively. As confirmed by analyses of both azimuths and the modified Ornstein-Zernike (MOZ) models, the voids were oblate ellipsoids with an average aspect ratio of 1.20, and voids with large dimensions lay within the compaction plane. Joseph et al. (2020)[90] further proposed that the voids were interconnected in the form of randomly oriented aggregates comprised of primary, non-spherical voids, forming a spatially correlated ramified structure. Christopher et al. (2021)[9] conducted in-situ SANS and USANS experiments on PBX 9502 under thermal cycling at a temperature of 25–220 °C to quantify the changes in the microstructure under elevated temperatures. They used a two-phase system of correlated ramified porosity with a MOZ model to interpret the USANS curves. The radius of gyration of the void correlation distance, the void radius of gyration, the volume and surface dimensions of the voids, and the void volume fraction derived from the Porod invariant in the PBX9502 were quantified as a function of temperature. Furthermore, they found the temperature dependence of the void radius of gyration was closely correlated with that of shock sensitivity, providing a microstructural origin for the increased shock sensitivity at elevated temperatures.

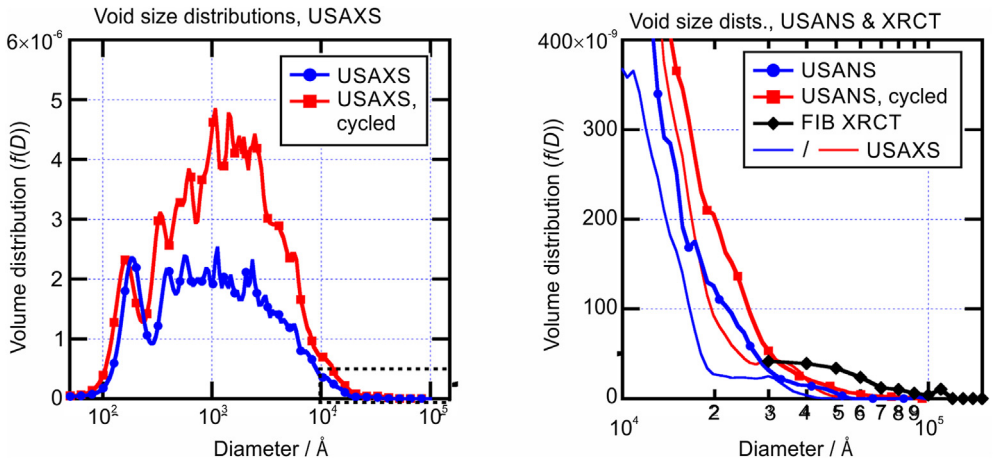

Fig. 5. Left pane: maximum-entropy derived void size distributions of LX 17 from the USAXS data. Right pane: an inset view of the left pane that focuses on the USANS and FIB-XRCT results.[120]

To evaluate the thermal stability of microstructures, Lin et al. (2021)[6] conducted in-situ SANS experiments on a series of PBX composites under the temperatures of 25–120 °C in 2021. They put forward a new method to process the in-situ SANS results, in which the temperature dependence of the SANS count rates and pseudo-invariant was roughly used to evaluate the thermal stability of microstructures. The in-situ SANS results clearly showed that the PDA coating could promote the microstructural thermal stability of PBXs, especially for TATB-based PBX materials.

Perry et al. (2018)[11] determined the void size distribution in the range of 1 nm–10 μm in PBX 9502 using USANS. They applied a bimodal lognormal model to parameterize the USANS results. Moreover, they incorporated the as-obtained void size distribution data into the building of the Scaled Uniform Reactive Front (SURF) burn model for the first time.

4.1.6. Porosity and microstructures of other PBX materials

In recent years, some other nanocrystalline PBX materials have been developed and investigated using SAS techniques to reveal their porosity or microstructures. Sanjay et al. (2010)[121] conducted the SAXS measurement of nanocrystalline trinitrotoluene (TNT)/silica xerogels and revealed that TNT entered the pores of the silica matrix, thus reducing the average pore size. Later, Sanjay et al. (2013)[122] performed similar experiments on nanostructured RDX/SiO_2 xerogel systems, demonstrating that RDX coexisted well with the pore network of silica matrix and the loading of RDX would reduce the size of primary particles.

Moreover, Victor et al. (2013)[123] performed USAXS measurement of nanostructured RDX/wax systems to reveal their porosity structure. The USAXS analysis showed that all RDX/wax materials exhibited bimodal, lognormal void size distributions, and the 200 nm, 500 nm, and FEM-grade RDX-based specimens had a mean void size of 280 nm, 550 nm, and 1300 nm, respectively. Furthermore, porosity was mainly attributed to voids with a size of greater than about 50 nm, and the voids were primarily enclosed by wax.

4.2. Interface characteristics derived from NR

Palmer et al. (1993)[124] and Rae et al. (2002)[3] found that cracks tend to occur at interfaces, as shown in Fig. 6. Crack formation is especially troubling for all the plastic-bonded explosives. As shown by the results of a series of studies,[3,124,125] cracks rarely cut through crystals but are generally confined to stiff binder samples, while the occurrence and growth of interfacial cracks are the dominant failure mode in general. Therefore, research on the evolution of the interfacial microstructure in the service and storage environments is significant for the validity determination and process improvement of PBXs.

Yeager et al. (2014) found that adding plasticizers to binders can influence the explosive crystal-binder interfaces in PBXs.[94] Most plasticizers are short-chain or monomer polymers and are more prone to diffuse throughout PBXs. When the temperature and humidity in the external environment change, plasticizers are easy to suffer interfacial aggregation in PBXs, hindering the formation of effective interfaces. After long-term storage, plasticizers are prone to migrate to the surface.

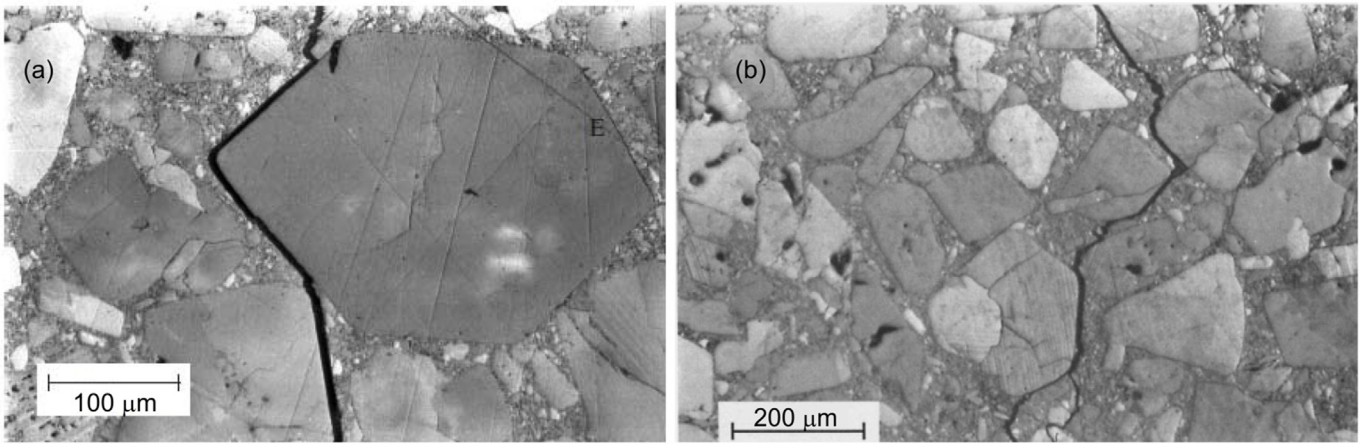

Fig. 6. Micrographs of PBX 9501 with cracks highlighted.[124]

As shown in Fig. 7, plasticizers hindered the interfacial diffusion in comparative experiments, thinning the interfaces. The nanoindentation experiment showed that the interfacial strength was reduced and cracks were easy to form. The microstructure parameters of two-phase interfaces can be obtained from NR, thus providing accurate parameter data for the subsequent nanoindentation experiments and conclusions.

Yeager et al. (2018)[95] carried out comparative experiments of a PBX 9404 sample, a heated PBX 9404 sample, and a sample treated with accelerated aging for two years using NR. As shown in Fig. 8, the three samples showed quite different interface microstructures. After heating or aging, the film structure changed greatly due to the evaporation of the plasticizers or the surface-interface migration. The NR could achieve thickness precision of 0.5 nm, thus yielding accurate interfacial structure. Precise microstructural parameters of interfaces can reveal important information inside different PBXs. The experiments allowed for establishing accurate relationships between the environmental temperature and humidity conditions, aging time, and the microstructure parameters of interfaces. These results provide important experimental parameters for process improvement and the design of new PBXs. Meanwhile, they also provide basic parameters for the selection and doping of binders.

In sum, the stability and performance of ultra-thin films in a service environment should be ascertained before utilization. NR is an effective and accurate tool to investigate the interfaces of explosive crystals and binders and corresponding parameters, which are very useful for enhancing the PBX performance.

4.3. ND-derived microstructures of explosive crystallites

The performance of solid energetic materials depends on several factors including the sensitivity to detonation by stimulus, detonation velocity, chemical reactivity, thermal stability, crystal density, and crystal morphology, which in turn are governed by the solid-state structure of the energetic materials.[126,127] Furthermore, energetic materials, which are molecular crystals in nature, have a low energy barrier for phase transition due to relatively weak intermolecular interactions, resulting in a common phenomenon of polymorphism. Different polymorphs lead to different physical properties, such as morphology, sensitivity, and energy density, which greatly affect the performance of energetic materials. Therefore, it is significant to obtain detailed structural information on energetic materials and clarify the variation in the structure during the thermal and mechanical processes, especially during the solid-state phase transitions. ND has been mainly used to characterize

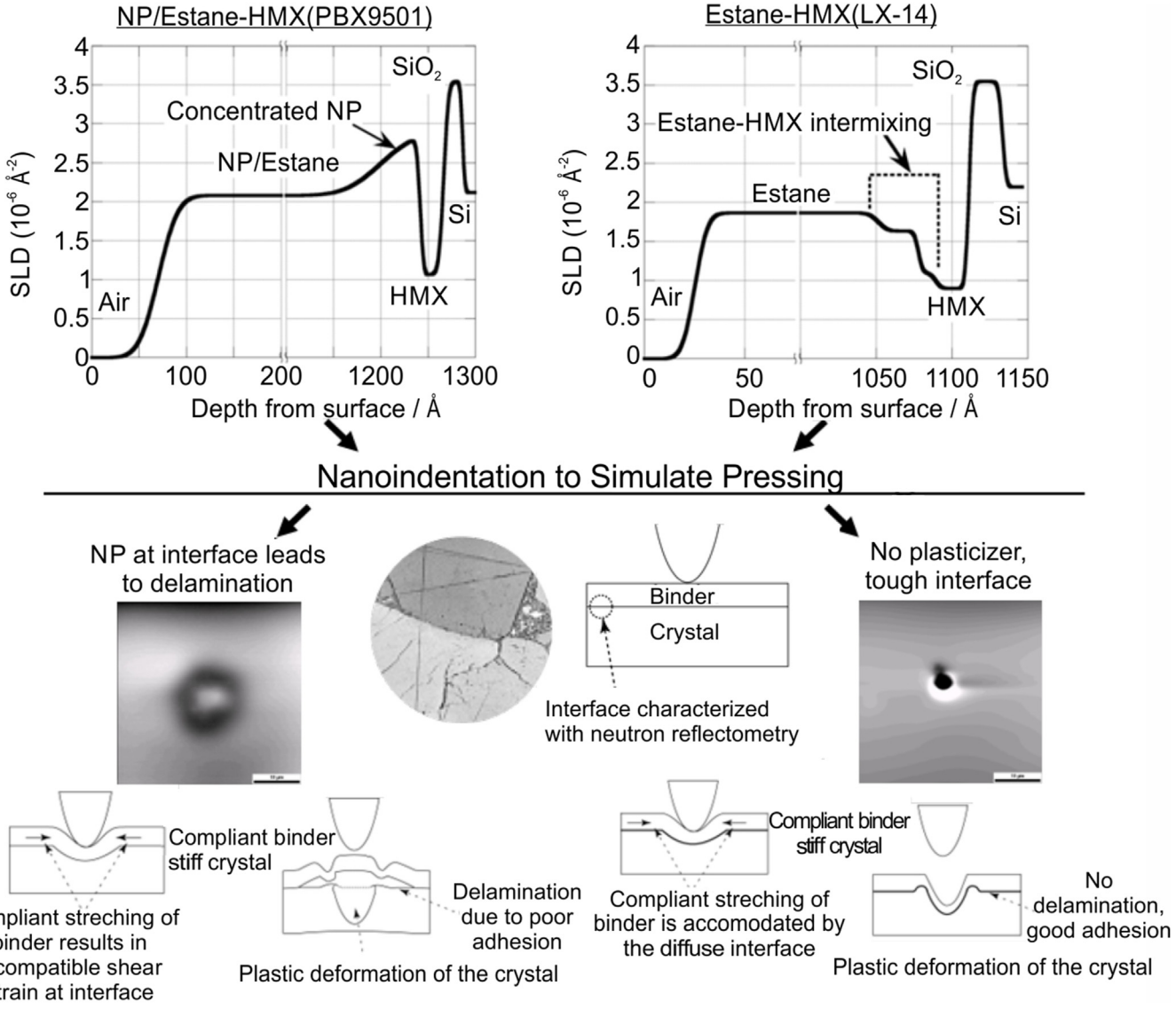

Fig. 7. SLD profiles of thin film samples of PBX 9501 and LX 14 and the corresponding experimental results of nanoindentation. Adding nitro-plasticizer alters interfaces and fracture mechanisms, thus favoring binder delamination.[94]

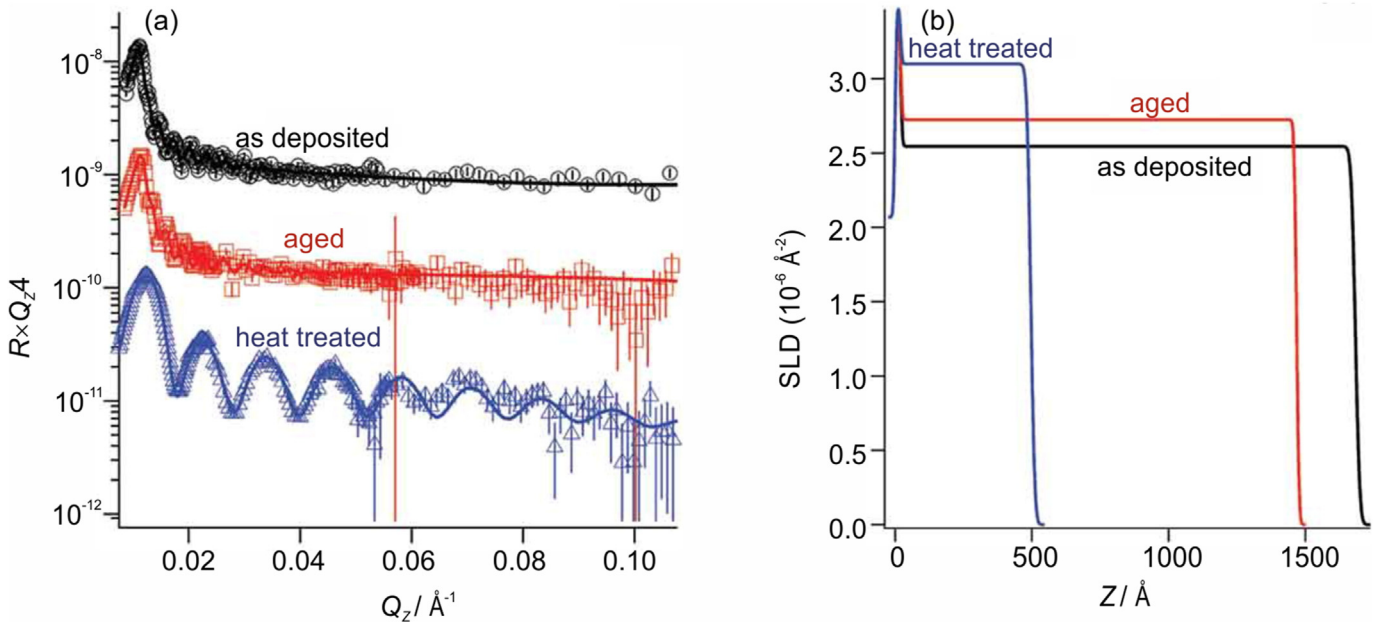

Fig. 8. Neutron reflectometry data and fitted results (a) along the SLD profile (b) for PBX 9404 binder film deposited on a silicon wafer. The effects of aging and heating showed similar trends, except that heating caused much more significant changes. In both cases, the film shrank and increased in SLD. This occurred due to the evaporation of the plasticizer from the film.[95]

the crystal structures and microstrains of explosives.

4.3.1. Crystal structures of explosive crystallites

As neutrons are relatively sensitive to hydrogen atoms, ND is a preferred technique for determining the positions of hydrogen atoms in energetic materials. The positions of hydrogen atoms in β-HMX were determined using single-crystal ND in 1970.[128] The positional and anisotropic thermal parameters of all atoms in β-HMX were measured using 551 reflections, which finally yielded an accurate result represented by a very low R-value of 0.059. With the precise ND data, the panoramic picture of β-HMX was entirely presented for the first time. All bond distances, bond angles, and anisotropic atomic displacement in β-HMX were determined, and the intra- and inter-molecular hydrogen bonds were also confirmed.

The high-pressure γ-form and high-pressure and high-temperature ε-form of RDX have been confirmed by combining X-ray with ND.[126,129,130] The transition from α-to γ-RDX phase is barely influenced by temperature, but temperature and pressure are important factors in the transition rate. The transition from α-to γ-RDX phase at ambient temperature occurs under pressure of 3.9 GPa.[129] It is interesting that molecular transformation occurs in this phase transition. The molecules in α-RDX exhibit one transformation, while those in γ-RDX exhibit two different transformations distinguished by the orientation of nitro groups. The high-pressure, high-temperature phase of RDX was taken as β-RDX in early studies due to the similarities of β- and ε-RDX in vibration spectra[131,132] until Millar spotted differences using neutron powder diffraction in 2009.[133] With the clue shared by Millar, Dreger found significant differences using Raman spectra, in which the frequency was either very low or very high – below 150 cm^{-1} (mainly lattice vibration and NO_2 rotation) and near 3000 cm^{-1} (C–H stretching).[134]

A new high-pressure phase of FOX-7 was indicated using neutron powder diffraction in 2015.[103] Before this, the structures of three ambient pressure phases α, β, and γ were provided.[135,136] Among them, α-FOX-7 (monoclinic, space group $P2_1/n$) is the most stable under ambient conditions. It transitions to β-FOX-7 (orthorhombic, space group $P2_12_12_1$) when being heated above 389 K and then to γ-FOX-7 (monoclinic, space group $P2_1/n$) when being heated above 446 K. The γ-FOX-7 presents a layered structure, causing a strong reflection corresponding to the interplanar distance between layers. The high-pressure phase of FOX-7 also includes a strong reflection, leading to an assumption that the high-pressure phase may be γ-FOX-7. Pravica speculated that the high-pressure form of FOX-7 could be γ- FOX-7.[137] However, neutron powder diffraction showed a significant difference between the new high-pressure phase and γ-FOX-7 (Fig. 9). Although the structure of this high-pressure phase is not available due to the absence of data on single-crystal diffraction or ultra-fine powder diffraction, the verification of a new phase is still great progress in the study of FOX-7 polymorphs.

CL-20 is one of the densest (2.04 g/cm^3) and the most energetic (detonation velocity: 9500 km/s) explosives at present. However, pure CL-20 has high sensitivity, making it unsafe in practical applications. ND is a relatively gentle way to study the crystallographic structural evolution of CL-20 since radiation damage to CL-20 has been observed when using synchrotron X-ray powder diffraction.[138] Similar phenomena frequently occur in small molecular materials upon synchrotron X-ray irradiation.[139] Radiation damage not only induces security problems but also brings uncertainty to experimental results. Lattice expansion was

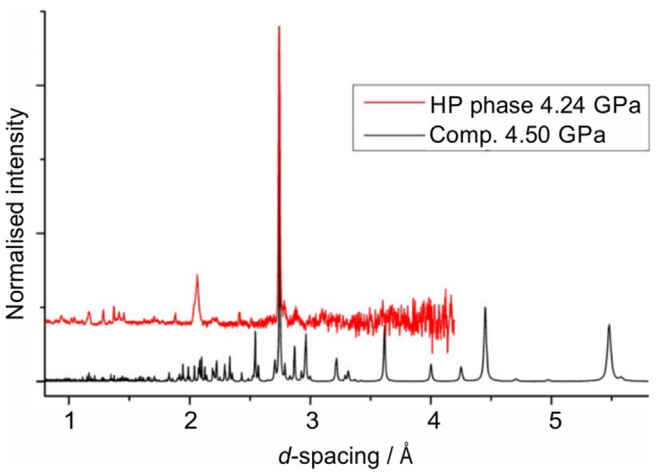

Fig. 9. Difference between experimental and theoretical neutron powder patterns of FOX-7.[103]

observed at retained pressure even after a short period in the study of ε-CL-20 (the densest and most stable form of CL-20 under the ambient condition) using synchrotron X-rays. This will influence the study of EOS as the volume is not solely dependent on pressure anymore. Besides, the high-pressure ND results of ε-CL-20 exhibit smooth compression behavior and agree well with theoretical prediction.[138]

Yeager et al. (2016)[48] studied in detail temperature-dependent variations in TATB loose powder and compressed pellets. The thermal cycling experiments using ND yielded results consistent with the XRD results of Sun et al.[140] The pellets were die-pressed neat TATB polycrystalline without polymer binders. Significant shrinking of the *c* axis was observed in the pellets compared with loose powders in ambient conditions, while slight expansion occurred in the *a* and *b* axes. Meanwhile, the pellets had a preferred crystal orientation aligning the (001) plane normal along the compression axis. These results are naturally related to the layered structure of TATB. Interestingly, a shift in the shape of the unit cell occurred in the pellets, which is different from the case of the loose powder. Besides the significant compression in the *c* axis and the subtle expansion in the *a* and *b* axes upon heating, the compression almost solely accounted for the change in the α angle of the unit cell, with only a slightly noticeable shift in β.

HMX has four known solid phases, namely α, β, γ, and δ. β-HMX is the most stable form in ambient conditions and can convert to δ-HMX when heated above 170 °C.[141] The δ-to β-HMX transition is accelerated in a humid atmosphere compared to a dry atmosphere and brings considerable defects due to changes in volume.[86] The γ-HMX might be the intermediate phase during δ-to β-HMX retransformation as γ-HMX is a hydrated phase. However, no evidence of γ-HMX has been found during δ-to β-HMX retransformation through ND and XRD.[47] This result is reasonable because γ-HMX is metastable in ambient conditions and retains for a long time unless contacting a solvent such as acetone. Therefore, γ-HMX cannot easily convert to β-HMX in the case of just exposure to air.[142,143] The theoretical study also shows that the energy barrier is larger from γ-to β-HMX than from δ-to β-HMX. This result indicates that direct retransformation from δ-to β-HMX is easier than the retransformation through the intermediate phase of γ-HMX.[144]

4.3.2. *Microstrains of energetic materials*

ND can also be used to study the microstrains in energetic materials. Strains are the quantitative description of deformations or distortions. When an object suffers tensile stress, its lattices expand in a related orientation, resulting in a positive strain. However, strains in practical polycrystalline samples are complicated as millions of single-crystal or multi-crystal particles exist in highly random orientations regardless of textures. The average strains in these particles can be measured using a diffraction method, but an average itself is not sufficient sometimes. Microstrains are described as the root-mean-square of strains, i.e., the fluctuation in strains. Therefore, microstrains correspond to the inhomogeneity of interplanar stress or molecular dislocation that can cause fluctuation in the interplanar distance. Therefore, microstrains can be derived by broadening reflections and are related to material defects.[145] Microstrains in special microstructures such as slip systems are noteworthy because deformation or distortion can be easily found in such locations. An in-situ ND study of HMX revealed a sudden decrease in microstrains in the (100) plane when powder samples were compressed to 380 MPa. This finding marks microcracks in HMX-based polycrystalline particles.[47] The (001) [100] is the dominant slip system in HMX lattices according to mechanical test results.[146] Thus, the microstrains of the (100) plane are related to the molecular dislocation in the slip orientation, which will lead to elevated lattice energy. Normally, an increase in external stimulus such as pressure will induce an increase in microstrains. This result is consistent with the ND observation of another plane of HMX.[47] The sudden decrease in microstrains in the (100) plane will release the energy brought by molecular dislocation in the (100) plane. A reasonable presumption is that microcracks propagate to the final stage (failure) at 380 MPa, under which stress starts to decrease.[147,148] As microstrains decrease in the slip orientation of the (001)[100] slip system, microcracks are presumed to be dominated by mode II cracks according to Griffith's theory.

A similar result was observed in a study of TATB using ND.[149] The low symmetry and rich textures of TATB make it difficult to conduct an anisotropic analysis. As TATB molecules exhibit a layered structure corresponding to the XY plane, the microstrain distribution on planes with Miller index $l = 0$ was studied using ND. A sudden decrease in the microstrains on the (100) plane (corresponding to the (001)[100] slip system) was observed at pressure of 570 MPa. It was uncertain whether the (001)[100] slip system predominated due to the absence of mechanical test results. Another interesting observation is that the microstrains were dominant on the (010) plane compared with other (*h k* 0) planes. This result indicates the interplanar shift of TATB molecules most probably occurred in the [010] direction. This may explain the unclear implication mentioned by Yeager, i.e., the change in α angle brought by compression was far more noticeable than that in β[48]. ND also revealed a diffraction peak division when TATB was compressed to 4 GPa.[149] This result implies the high-pressure phase transition of TATB, as a similar viewpoint was reported from single-crystal XRD.[150] However, powder XRD studies showed that TATB retained its ambient lattice structure up to 66 GPa.[151,152] The rich textures of TATB under high pressure due to its layered structure is the main factor for disagreement. Whether a first-order phase transition of TATB exists at pressure of nearly 4 GPa still needs to be verified using high-quality diffraction data.

Significant progress has been made in the study of the polymorphs and EOS of energetic materials using diffraction methods. Nevertheless, there are still many questions to be solved. For example, the high-pressure phase structure of numerous energetic materials is not yet determined. Furthermore, mechanical failure is also an important problem in the application of solid energetic materials. All these require further scientific studies and new diffraction and correlative techniques.

5. Discussion and outlook

As summarized in the above sections, scattering techniques have been widely used to quantify the complex, diverse, and multi-scale microstructures of various PBXs. Since these techniques have their own advantages and limitations, their combination for characterizing PBX materials is discussed and some promising subjects for their further applications are proposed.

5.1. *Combination of different techniques for characterizing PBX materials*

Two limitations exist in the application of SAS techniques to PBX materials. The first limitation is that all the acquired data or conclusions from SAS experiments should fall into the measurement ranges of length scale or *Q*. This limitation directly influences the physical meaning of the measured void size distribution, void volume fraction, and the limit of detectable correlated lengths or void radii. As revealed by Trevor et al. (2006),[42] the void volume of a compact UFTATB sample obtained from the USAXS experiment changed insignificantly but its bulk volume increased by 0.6% after 2.5 cycles at a temperature of -55–70 °C, indicating some increased voids were beyond the sensitivity of USAXS. The second limitation is that the interpretation of SAS data for PBX materials is ambiguous due to the absent phase information in Fourier scattering space and the inherently sophisticated microstructures. Therefore, the acquired void morphologies and numeric values about the size and quantity of voids should be correlated. According to Joseph et al. (2010),[50] the void size distributions and binder-filled regions were obtained through the modeling of the USANS data, which were assumed to be spherical and cylindrical in shape, but it was impossible to determine the shape using USANS alone. Another example is that different models of void structures for PBX 9502 have been proposed,[42,90] including the void size distribution extracted from the maximum entropy algorithm under the spherical form assumption, the ramified void structures

described using the modified Ornstein-Zernike (MOZ) model, and the aggregates comprised of non-spherical, primary voids with an aspect ratio of 1.20.

Given the above limitations, the combination of different methods is highly crucial to the accurate or effective application of the SAS techniques to PBX materials. The first combined method is the facile combination of SANS, USANS, SAXS, and USAXS used to get a broad *Q* range and adequate scattering contrast variation.[15,90] This combination has been applied to mechanically induced PBX composites and the ratchet growth of LX 17, PBX 9501, and PBX 9502. The second combined method is the combination of SAS techniques with imaging methods, including optical microscopy,[8] scanning electron microscopy,[22–24] and x-ray computed tomography based on a focused ion beam (FIB) instrument or synchrotron.[15] This combined method can be used to extend the range of observed structural sizes to centimeters and validate the as-obtained inferences in real space. This method has been applied to determining the fractal scattering features of the voids in RDXs,[8] proposing the non-spherical voids in PBX 9502, providing the structural features of voids in LX 17 from 10 nm to 1 cm[15], and determining the microstructural features of nano-structured RDXs in SiO_2 xerogels.[122] The third is the combination of SAS techniques with Brunauer-Emmett-Teller (BET) measurements[37,89] and magnetic resonance.[153] The specific surface areas of explosive crystallites obtained using BET and SAS techniques have been frequently integrated to ascertain the SAS results or infer more details. Magnetic resonance has been widely used to characterize the porosity of shales,[153] serving as a great reference for PBX systems.

For NR applications, all the samples should be specially prepared ultra-thin films with a very smooth surface, and the data on the microstructure of the obtained interface should be averaged in the direction parallel to the surface plane. Therefore, the combination of NR with X-ray reflectivity, SEM, ellipsometry, atomic force microscopy, and nano-indentation is very important for accurately interpreting the reflection results, explaining the mechanisms of interfacial delamination, and building interfacial diffuse models, just as shown in relevant literature. For ND applications, the combination of diffraction methods (e.g., ND and XRD) with vibration methods (e.g., Raman and infrared spectrum) is highly effective in the study of phase transition. Diffraction methods concern the crystal structure and can reveal the structural changes during first order phase transitions. By contrast, vibration methods are sensitive to second order phase transitions, in which changes in vibrational modes usually occur. Neutrons interact primarily with atomic nuclei, while X-ray interacts primarily with the electron cloud surrounding atoms. Therefore, the combination of ND and XRD has been proposed to identify the differences between nuclear and electronic density distribution, which will benefit the study of polarity.

5.2. Some promising subjects

This review mainly summarized the applications of scattering techniques, including SAS, NR, and ND, in the microstructural characterization of PBX composite materials and explosive crystallites. These applications have yielded many quantitative parameters about the multi-scale microstructures, lots of insights into the microstructural evolution under thermal cycling and mechanical loads, some conclusions about the dependence of microstructures on preparation conditions, and weak correlations between microstructural features and properties. Nonetheless, efforts should be paid to the following promising subjects or important trends.

The first promising subject is to further gather the systemic and comprehensive microstructural parameters derived using scattering techniques for certain industrial PBX composite materials and explosive crystallites obtained from mass production and to add them to corresponding characteristic databases. The reported parameters in publications are a little disordered and dispersive especially when the sample conditions are discrepant, hindering the achievement of solid correlations between structures and properties. For example, some special batches of explosive crystallites (e.g., HMX, TATB, LLM-105, RDX, and nano-TATB) and vital PBXs with special formulations can be thoroughly characterized using methods such as SAS, CV-SAS, and XR-CT based on the same batches of specimens. These results can be used as the basic morphology data accompanied by preparation conditions. This subject is a meaningful challenge because of the safety problem resulting from the intrinsic hazards of energetic materials, different sample requirements, and an inaccessible testing chance of the above characterization techniques.

The second promising subject is to further investigate the dependence of the microstructural features of PBX composite materials and explosive crystallites on the preparation conditions or post-treatment processes. Some examples include the microstructural comparison between new and legacy TATBs and among RDX and DAAF powders from different manufacturers during the thermal cycling of TATB-based PBXs, during the heating process of PBX9404, during the high-pressure compression of HMX and TATB, and during the accelerated aging process of nano-TATB. These are ideal instances of other newly concerned sample systems.

The third promising subject is to further establish multi-factor correlations between the multi-scale microstructural features derived using scattering techniques and multiple performances obtained from experiments, which may include mechanical response, ratchet growth, various sensibilities, and detonation performance. Some scholars have completed preliminary studies of this subject. For instance, Thompson et al. (2010)[4] explained the differences in the mechanical response of PBX 9502 using the void structures, Chad et al. (2010)[8] correlated the scattering pseudo-invariant of voids with the shock sensitivity of RDX crystallites, Yeager et al. (2012)[12] explained the contrasting delamination behaviors of HMX/estane films using the interfacial diffusion structure, Joseph et al. (2013)[91] correlated the fractal structure of voids with the transitions between brittleness and ductileness of TATB crystallites, He et al. (2020) explained the mechanical response of the multilevel core-shell structured TATB-based PBX using the interface fractal dimensions, Christopher et al. (2021)[9] correlated the void radius of gyration with the run-to-detonation distance of heated PBX 9502. Some of these obtained relationships are a little weak or not rigid and also lack correlations with other performances (e.g., flyer initiating). Therefore, further investigations are required.

The fourth promising subject is to further incorporate the microstructural parameters derived from scattering techniques into various theoretical computational models in order to elucidate multi-scale mechanisms, predict performances, and assess the lifetime of PBX composite materials and explosive crystallites. The only two successful examples in this aspect are as follows: Trevor et al. (2009)[5] explained the change in the void size distribution behind ratchet growth using the coarse-grained mesoscale model. Perry et al. (2018)[11] incorporated the void size distribution obtained using USANS into the building of the Scaled Uniform Reactive Front (SURF) burn model.

The fifth promising subject is to further incorporate the as-obtained correlations or understandings into the design principle of PBX formulations and the optimization of the preparation and post-treatment processes to reduce the development period and cost of PBXs, just as Trevor et al. (2009)[120] proposed achieving next generation of PBX materials.

Besides, some other subjects about promoting the scattering theory and techniques for PBX materials also deserve attention. Some other types of scattering techniques can be applied,[154] such as the spin-echo SANS, which can be used to obtain the real-space correlation function, and the spin-echo inelastic scattering, which can be used to obtain certain dynamic information. More types of in-situ environment equipment or techniques should be developed, such as in-situ devices that are coupled with temperature and aerostatic pressure for composite PBXs, coupled with temperature and mechanical loading for composite PBXs, coupled with temperature and uniaxial compaction for modeling powders, and coupled with temperature and humidity for nano-structured explosive crystallites. More types of data fitting methods or algorithms for the scattering results of PBX materials should be developed, such as the

methods for modeling slit-smeared USAS data combined with pinhole-smeared SANS data, the methods for fitting SAS results based on the computer-aided construction of three-dimensional structures, and the methods for combining the results obtained using scattering techniques and other complementary tools. In addition, it is necessary to develop some techniques for the easy and efficient implementation of the scattering experiments of PBXs materials, including the methods for sample preparation, component deuteration, and automated testing and analysis.

6. Conclusions

Based on large scientific facilities for characterizing multi-scale microstructures of PBX materials, this review mainly introduced the principles and typical applications of SAS, NR, and ND and available instruments in China. It also presented a simple discussion about the combination of scattering techniques with other methods, as well as some promising subjects for the further applications of these techniques. The following conclusions can be drawn from this review.

(1) The scattering techniques based on large scientific facilities can provide many quantified parameters of the microstructural features of PBX materials. SAS and USAS instruments can help obtain the size distribution and content of (internal or external) voids in the range of 1 nm–20 μm, the specific interfacial area, and the fractal structures of voids or interfaces of PBX composites and explosive crystallites. Neutron reflection can yield the thickness and the interfacial diffusion structures of bi-films of explosive crystallites and binders. ND can provide the crystal structures and microstrains of PBX composites and explosive crystallites.
(2) The above scattering techniques can be easily combined with various environment instruments and thus are convenient for in-situ temperature cycling, mechanical loading, solution, and other atmosphere filling experiments. Therefore, the in-situ thermal cycling experiments are mostly performed for PBX materials.
(3) Efforts have been made to correlate as-obtained microstructural parameters obtained using scattering with various performances or properties, including mechanical responses, ratchet growth behavior, various sensibilities, and detonation performance, and incorporate them into theoretical computational models. Some interesting insights or mechanisms have been proposed and deserve further efforts.
(4) With the rapid increase in the available scattering techniques for PBX materials based on large scientific facilities, more opportunities are provided to the energetic material community.

Author contribution

Liang-fei Bai contributed to the review of SAS and the whole manuscript preparation. Xin-xi Li contributed to the review of NR. Hao Li contributed to the review of ND. Pro. Guang-ai Sun contributed to the design and implementation of the review. Dong Liu contributed to the review of large scientific facilities in China. Zhan-yu Wu contributed to the literature search on USANS. Mei Peng contributed to the literature search on USAXS. Zhi-chao Zhu contributed to the literature search on SANS. Chao-qiang Huang contributed to the literature search on NR. Fei-yan Gong contributed to the literature search on TATB-based PBXs. Shi-chun Li contributed to the literature search on SAXS.

Declaration of competing interest

The authors declare that they have no known competing financial interests or personal relationships that could have appeared to influence the work reported in this paper.

Acknowledgments

The authors acknowledge all the neutron scattering colleagues from the CMRR for their enormous contributions and great support to this review. The authors' thanks also go to Dr. Ben-qiong Liu and Dr. Chang-Sheng Zhang for their help in English writing. This work was partially funded by the National Natural Science Foundation of China (U2130207), the CAEP Foundation (CX20210027) and the National Natural Science Foundation of China (U1730244, 12105264).

References

1. Yan QL, Nie FD, Yang ZJ. *Polymer Bonded Explosives and Their Properties*. In: National Defense Industry Press; 2020.
2. Asay B. *Shock Wave Science and Technology Reference Library*. Vol. 5: non-shock initiation of explosives. Vol 5: Springer Science & Business Media; 2009.
3. Rae PJ, Palmer SJP, Goldrein HT, Field JE, Lewis AL. Quasi-static studies of the deformation and failure of PBX 9501. *P Roy Soc a-Math Phy*. 2002;458(2025): 2227–2242.
4. Thompson DG, Brown GW, Olinger B, et al. The effects of TATB ratchet growth on PBX 9502. *Propellants, Explos Pyrotech*. 2010;35(6):507–513.
5. Willey TM, Hoffman DM, van Buuren T, et al. The microstructure of TATB-based explosive formulations during temperature cycling using ultra-small-angle X-ray scattering. *Propellants, Explos Pyrotech*. 2009;34(5):406–414.
6. Lin CM, Gong FY, Qian W, et al. Tunable interfacial interaction intensity: construction of a bio-inspired interface between polydopamine and energetic crystals. *Compos Sci Technol*. 2021;211, 108816.
7. He GS, Li X, Bai LF, et al. Multilevel core-shell strategies for improving mechanical properties of energetic polymeric composites by the "grafting-from" route. *Compos B Eng*. 2020;191, 107967.
8. Stoltz CA, Mason BP, Hooper J. Neutron scattering study of internal void structure in RDX. *J Appl Phys*. 2010;107(10), 103527.
9. Armstrong CL, Mang JT. Thermally-driven changes to porosity in TATB-based high explosives. *Propellants, Explos Pyrotech*. 2021;46(8):1304–1312.
10. Berghout HL, Son SF, Skidmore CB, Idar DJ, Asay BW. Combustion of damaged PBX 9501 explosive. *Thermochim Acta*. 2002;384(1):261–277.
11. Perry WL, Clements B, Ma X, Mang JT. Relating microstructure, temperature, and chemistry to explosive ignition and shock sensitivity. *Combust Flame*. 2018;190: 171–176.
12. Yeager JD, Ramos KJ, Singh S, Rutherford ME, Majewski J, Hooks DE. Nanoindentation of explosive polymer composites to simulate deformation and failure. *Mater Sci Tech-Lond*. 2012;28(9-10):1147–1155.
13. Handley C, Lambourn B, Whitworth N, James H, Belfield W. Understanding the shock and detonation response of high explosives at the continuum and meso scales. *Appl Phys Rev*. 2018;5(1), 011303.
14. Armstrong CL. *Effects of Void Morphology on Detonation Initiation of PBX 9502*. Los Alamos, NM (United States): Los Alamos National Lab. (LANL); 2020. LA-UR-20-23230.
15. Willey TM, Lauderbach L, Gagliardi F, et al. *Comprehensive Characterization of Voids and Microstructure in TATB-Based Explosives from 10 Nm to 1 Cm: Effects of Temperature Cycling and Compressive Creep*. Livermore, CA (United States): Lawrence Livermore National Lab.(LLNL); 2010. LLNL-PROC-425116.
16. Mang JT, Skidmore CB, Son SF, Hjelm RP, Rieker TP. An optical microscopy and small-angle scattering study of porosity in thermally treated PBX 9501. *AIP Conf Proc*. 2002;620:833–836.
17. Peterson PD, Mang JT, Asay BW. Quantitative analysis of damage in an octahydro-1,3,5,7-tetranitro-1,3,5,7-tetrazonic-based composite explosive subjected to a linear thermal gradient. *J Appl Phys*. 2005;97, 093507.
18. Bai LF, Tian Q, Tu XQ, et al. SANS investigation on the effect of cold-pressed forming pressure on the microstructure of HMX-based PBX. *Chin J Energetic Mater*. 2019;27(10):853–860.
19. Skidmore CB, Phillips DS, Crane NB. *Microscopical Examination of Plastic-Bonded Explosives*. Los Alamos, NM (United States): Los Alamos National Lab.(LANL); 1997. LA-UR-97-2738.
20. Liu JH, Liu SJ, Huang M, Li HZ, Nie FD. Progress on crystal damage in pressed polymer bonded explosives. *Chin J Energetic Mater*. 2013;21(3):372–378.
21. Xu RJ, Kang B, Huang H, Li JS, Jiang Y, He F. Crystal quality and properties of spherical HMX. *Chin J Energetic Mater*. 2008;16(2):149–152.
22. Mulford RN, Romero JA. Sensitivity of the TATB-based explosive PBX-9502 after thermal expansion. *AIP Conf Proc*. 1998;429:723–726.
23. Peterson P, Mang J, Fletcher M, Olinger B, Roemer E. Influence of pressing parameters on the microstructure of PBX 9501. *AIP Conf Proc*. 2004;706:796–799.
24. Hoffman DM, DePiero SC. *Characterization and Qualification of New TATB and Kel-F 800 for LX-17*. Livermore, CA (United States): Lawrence Livermore National Lab.(LLNL); 2007. UCRL-TR-228232.
25. Proud WG, Palmer SJP, Field JE, Kennedy G, Lewis A. AFM studies of PBX systems. *Thermochim Acta*. 2002;384(1):245–251.
26. Lin CM, He GS, Liu JH, Pan LP, Liu SJ. Construction and thermal properties of nano-structured polymer bonded explosives with graphene. *RSC Adv*. 2015;5(119): 98514–98521.

27. He GS, Liu JH, Gong FY, Lin CM, Yang ZJ. Bioinspired mechanical and thermal conductivity reinforcement of highly explosive-filled polymer composites. *Compos Appl Sci Manuf*. 2018;107:1–9.
28. Lin CM, He GS, Liu JH, et al. Construction and non-linear viscoelastic properties of nano-structure polymer bonded explosives filled with graphene. *Compos Sci Technol*. 2018;160:152–160.
29. Liu R, Li M, Li JM. Modeling the damage evolution in compressed polymer bonded explosives based on computed microtomography images. *Sci Technol Energetic Mater*. 2013;74(1):29–33.
30. Manner VW, Yeager JD, Patterson BM, et al. In situ imaging during compression of plastic bonded explosives for damage modeling. *Materials*. 2017;10(6):638.
31. Willey TM, Lauderbach L, Overturf G. *Binder Mixing and Concentration Variation in TATB Polymer-Bound Explosives*. Livermore, CA (United States): Lawrence Livermore National Lab.(LLNL); 2014. LLNL-PROC-656400.
32. Zhang WB, Yang XH, Yang RC, Feng LY, Yang CF. X-ray Micro-tomography of TATB Based Polymer Bonded Explosives under Unidirectional Warm die Compaction. *Chin J Energetic Mater*. 2014;22(2):202–205.
33. Zhang WB, Tian Y, Yong L, Yang XH, Dai B, Li JM. X-ray microtomography of TATB granules under isostatic warm soft compaction. *Chin J Energetic Mater*. 2018;26(9):779–785.
34. Bailey A, Bellerby J, Kinloch S. The identification of bonding agents for TATB/HTPB polymer bonded explosives. *Philos Trans R Soc London, Ser A: Physical Engineering Sciences*. 1992;339(1654):321–333.
35. Zhu Q, Xiao C, Li SB, Luo G. Bioinspired fabrication of insensitive HMX particles with polydopamine coating. *Propellants, Explos Pyrotech*. 2016;41(6):1092–1097.
36. Borne L, Patedoye JC, Spyckerelle C. Quantitative characterization of internal defects in RDX crystals. *Propellants, Explos Pyrotech*. 1999;24(4):255–259.
37. Mang JT, Skidmore CB, Hjelm RP, Howe PM. Application of small-angle neutron scattering to the study of porosity in energetic materials. *J Mater Res*. 2000;15(5):1199–1208.
38. Borne L, Herrmann M, Skidmore CB. *Microstructure and Morphology*. In: Energetic Materials; 2005:333–366.
39. Lin CM, Liu JH, He GS, et al. Non-linear viscoelastic properties of TATB-based polymer bonded explosives modified by a neutral polymeric bonding agent. *RSC Adv*. 2015;5(45):35811–35820.
40. Yang ZJ, Ding L, Wu P, Liu YG, Nie FD, Huang FL. Fabrication of RDX, HMX and CL-20 based microcapsules via in situ polymerization of melamine–formaldehyde resins with reduced sensitivity. *Chem Eng J*. 2015;268:60–66.
41. Lin CM, Tian Q, Chen KP, et al. Polymer bonded explosives with highly tunable creep resistance based on segmented polyurethane copolymers with different hard segment contents. *Compos Sci Technol*. 2017;146:10–19.
42. Willey TM, van Buuren T, Lee JRI, et al. Changes in pore size distribution upon thermal cycling of TATB-based explosives measured by ultra-small angle X-ray scattering. *Propellants, Explos Pyrotech*. 2006;31(6):466–471.
43. Yan GY, Tian Q, Liu JH, et al. The microstructural evolution in HMX based plastic-bonded explosive during heating and cooling process: an in situ small-angle scattering study. *Cent Eur J Energ Mater*. 2016;13(4):916–926.
44. Luscher DJ, Yeager JD, Clausen B, Vogel SC, Higginbotham Duque AL, Brown DW. Using neutron diffraction to investigate texture evolution during consolidation of deuterated triaminotrinitrobenzene (d-TATB) Explosive Powder. *Crystals*. 2017;7(5):138.
45. Williams CE, May RP, Guinier A. Small-angle scattering of X-rays and neutrons. *X-ray Characterization of Materials*. 1999:211–254.
46. Sun MD, Zhao JL, Pan ZJ, et al. Pore characterization of shales: a review of small angle scattering technique. *J Nat Gas Sci Eng*. 2020;78, 103294.
47. Li H, Li Y, Bai LF, et al. Acceleration of delta- to beta-HMX-D8 phase retransformation with D2O and intergranular strain evolution in a HMX-based polymer-bonded explosive. *J Phys Chem C*. 2019;123(12):6958–6964.
48. Yeager JD, Luscher DJ, Vogel SC, Clausen B, Brown DW. Neutron diffraction measurements and micromechanical modelling of temperature-dependent variations in TATB lattice parameters. *Propellants, Explos Pyrotech*. 2016;41(3):514–525.
49. Pynn R. *Neutron Scattering—A Non-destructive Microscope for Seeing inside Matter*. In: Neutron applications in earth, energy and environmental sciences. Springer; 2009:15–36.
50. Mang JT, Hjelm RP, Francois EG. Measurement of porosity in a composite high explosive as a function of pressing conditions by ultra-small-angle neutron scattering with contrast variation. *Propellants, Explos Pyrotech*. 2010;35(1):7–14.
51. Mang JT, Hjelm RP. Small-angle neutron scattering and contrast variation measurement of the interfacial surface area in PBX 9501 as a function of pressing intensity. *Propellants, Explos Pyrotech*. 2011;36(5):439–445.
52. lightsources.org. https://lightsources.org/lightsources-of-the-world/.
53. FRM II. https://neutronsources.org/neutron-centres/.
54. Jiang XM, Tang ES, Xian DC. Beijing synchrotron-radiation facility. *Rev Sci Instrum*. 1995;66(2):2343–2348.
55. Li ZH, Wu ZH, Mo G, Xing XQ, Liu P. A small-angle X-ray scattering station at beijing synchrotron radiation facility. *Instrum Sci Technol*. 2014;42(2):128–141.
56. He DH. Hefei national synchrotron radiation source. *Wuli*. 1992;21(5):257–262.
57. Hu QD. Preface to the special issue: application of synchrotron radiation in materials research. *Acta Metall Sin-Engl*. 2022;35(1):1–2.
58. Yin LX, Tai RZ, Wang D, Zhao ZT. Progress and future of shanghai synchrotron radiation facility. *Journal of the Vacuum Society of Japan*. 2016;59(8):198–204.
59. Hua WQ, Wang YZ, Zhou P, et al. Microfocus small-angle X-ray scattering at SSRF BL16B1. *Chin Phys C*. 2017;41(4), 048001.
60. Li YW, Liu GF, Wu HJ, et al. BL19U2: small-angle X-ray scattering beamline for biological macromolecules in solution at SSRF. *Nucl Sci Tech*. 2020;31(12):117.
61. Song PQ, Zhang JQ, Li YW, Liu GF, Li N. Solution small-angle scattering in soft matter: application and prospective. *Hua Hsueh Hsueh Pao*. 2022;80(5):690–702.
62. Chen ZJ, Li H, Li CR, et al. Shear-induced alignment of low-aspect-ratio nanorods for modulations of multiple optical properties. *J Mater Chem C*. 2022;10(25):9478–9483.
63. Chen DF, Liu YT, Wu MM. The neutron scattering program at the China advanced research reactor (CARR): a progress report. *Neutron News*. 2009;20(2):32–35.
64. Ke YB, He CY, Zheng HB, et al. The time-of-flight small-angle neutron spectrometer at China spallation neutron source. *Neutron News*. 2018;29(2):14–17.
65. Zuo TS, Cheng H, Chen YB, Wang FW. Development and prospects of very small angle neutron scattering (VSANS) techniques. *Chin Phys C*. 2016;40(7), 076204.
66. Chen J, Kang L, Lu HL, Luo P, Wang FW, He LH. The general purpose powder diffractometer at CSNS. *Phys B Condens Matter*. 2018;551:370–372.
67. Zhu T, Zhan XZ, Xiao SW, et al. The multipurpose reflectometer at CSNS. *Neutron News*. 2018;29(2):11–13.
68. Zhang HX, Cheng H, Yuan GC, et al. Thirty meters small angle neutron scattering instrument at China advanced research reactor. *Nucl Instrum Methods A*. 2014;735:490–495.
69. Sun GA, Zhang CS, Chen B, Gong J, Peng SM. A new operating neutron scattering facility CMRR in China. *Neutron News*. 2016;27(4):21–26.
70. Peng SM, Peng TP, Sun GA. Progress on nuclear analysis techniques. *Nuclear Analysis*. 2022;1(1), 100007.
71. Song JM, Luo W, Liu BQ, et al. Kunpeng: a cold neutron triple -axis spectrometer at CMRR in China. *Nucl Instrum Methods A*. 2020;968, 163929.
72. Xu JP, Xia YG, Li ZD, et al. Multi-physics instrument: total scattering neutron time-of-flight diffractometer at China Spallation Neutron Source. *Nucl Instrum Methods A*. 2021;1013, 165642.
73. Luo T, He Z, Cheng H, et al. A new laser-based alignment method for the multi-slits VSANS in high precision. *Nucl Instrum Methods A*. 2021;1010, 165526.
74. Zhang J, Xia YH, Wang Y, et al. High resolution neutron diffractometer HRND at research reactor CMRR. *J Instrum*. 2018;13, T01009.
75. Li J, Wang H, Sun GG, et al. Neutron diffractometer RSND for residual stress analysis at CAEP. *Nucl Instrum Methods A*. 2015;783:76–79.
76. Xie L, Chen XP, Fang LM, et al. Fenghuang: high-intensity multi-section neutron powder diffractometer at CMRR. *Nucl Instrum Methods A*. 2019;915:31–35.
77. Peng M, Sun LW, Chen L, et al. A new small-angle neutron scattering spectrometer at China Mianyang research reactor. *Nucl Instrum Methods A*. 2016;810:63–67.
78. Li XX, Huang CQ, Wang Y, et al. Diting: a polarized time-of-flight neutron reflectometer at CMRR reactor in China. *Eur Phys J A*. 2016;131(11):407.
79. Li H, Wang S, Cao C, Huo HY, Tang B. Neutron imaging development at China Academy of engineering physics (CAEP). *Neutron Imaging for Applications in Industry and Science*. 2017;88:154–161.
80. Wang TT, Tu XQ, Wang Y, Li XX, Gong J, Sun GA. Design and simulations of spin-echo small angle neutron scattering spectrometer at CMRR. *Nucl Instrum Methods A*. 2022;1024, 166041.
81. Chen L, Sun LW, Tian Q, et al. Upgrade of a small-angle neutron scattering spectrometer Suanni of China Mianyang research reactor. *J Instrum*. 2018;13, P08025, 08.
82. Hamley IW. *Small-angle scattering: theory, instrumentation, data, and applications*. John Wiley & Sons; 2021.
83. Mang JT, Skidmore CB, Howe PM, Hjelm RP, Rieker TP. *Structural Characterization of Energetic Materials by Small Angle Scattering*. vol. 505. 2000:699–702, 1.
84. Mang JT, Sk, idmore CB, Green R. *Small-angle X-Ray Scattering Study of Inter Granular Porosity in a Pressed Powder of TATB*. Los Alamos, NM (United States): Los Alamos National Lab. (LANL); 2000. LA-UR-00-5343.
85. Willey TM, Lauderbach L, Gagliardi F, et al. Mesoscale evolution of voids and microstructural changes in HMX-based explosives during heating through the beta-delta phase transition. *J Appl Phys*. 2015;118(5), 055901.
86. Yan GY, Fan ZJ, Huang SL, et al. Phase retransformation and void evolution of previously heated HMX-based plastic-bonded explosive in wet air. *J Phys Chem C*. 2017;121(37):20426–20432.
87. Shi J, Liu JH, Bai LF, Yan GY, Duan XH, Tian Q. Microstructure of HMX crystallites studied by in situ variable-temperature small-angle X-ray scattering. *Chin J Energetic Mater*. 2020;28(9):848–853.
88. Tian Q, Yan GY, Bai LF, et al. Progress in the applied research of small-angle scattering technique in polymer bonded explosives. *Chin J Energetic Mater*. 2019;27(5):434–444.
89. Song PQ, Tu XQ, Bai LF, et al. Contrast variation small angle neutron scattering investigation of micro- and nano-sized TATB. *Materials*. 2019;12(16):2606.
90. Mang JT, Hjelm RP. Preferred void orientation in uniaxially pressed PBX 9502. *Propellants, Explos Pyrotech*. 2020;46(1):67–77.
91. Mang JT, Hjelm RP. Fractal networks of inter-granular voids in pressed TATB. *Propellants, Explos Pyrotech*. 2013;38(6):831–840.
92. Metelev SV, Pleshanov NK, Menelle A, et al. The study of oxidation of thin metal films by neutron reflectometry. *Physica B*. 2001;297(1-4):122–125.
93. Yeager JD, Dubey M, Wolverton MJ, et al. Examining chemical structure at the interface between a polymer binder and a pharmaceutical crystal with neutron reflectometry. *Polymer*. 2011;52(17):3762–3768.

94. Yeager JD, Ramos KJ, Hooks DE, Majewski J, Singh S. *Formulation-derived Interface Characteristics Contributing to Failure in Plastic-Bonded Explosive Materials*. Los Alamos, NM (United States): Los Alamos National Lab.(LANL); 2014. LA-UR-14-24860.
95. Yeager JD, Watkins EB, Duque ALH, Majewski J. The thermal and microstructural effect of plasticizing HMX-nitrocellulose composites. *J Energetic Mater*. 2018;36(1):13–28.
96. Festa G, Andreani C, Arcidiacono L, Grazzi F, Senesi R. Chapter 4 - neutron diffraction and (n, γ)-based techniques for cultural heritage. In: Lazzara G, Fakhrullin R, eds. *Nanotechnologies and Nanomaterials for Diagnostic, Conservation and Restoration of Cultural Heritage*. Elsevier; 2019:61–77.
97. Rietveld HM. The Rietveld method. *Phys Scripta*. 2014;89(9), 098002.
98. Enzo S, Fagherazzi G, Benedetti A, Polizzi S. A profile-fitting procedure for analysis of broadened X-ray-diffraction peaks .1. Methodology. *J Appl Crystallogr*. 1988;21:536–542.
99. Frontera C, Rodriguez-Carvajal J. FULLPROF as a new tool for flipping ratio analysis: further improvements. *Phys B Condens Matter*. 2004;350(1-3):E731–E733.
100. Cui J, Huang Q, Toby BH. Magnetic structure refinement with neutron powder diffraction data using GSAS: a tutorial. *Powder Diffr*. 2006;21(1):71–79.
101. Rietveld HM. A profile refinement method for nuclear and magnetic structures. *J Appl Crystallogr*. 1969;2:65–71.
102. Millar DIA, Marshall WG, Oswald IDH, Pulham CR. High-pressure structural studies of energetic materials. *Crystallogr Rev*. 2010;16(2):115–132.
103. Hunter S, Coster PL, Davidson AJ, et al. High-pressure experimental and DFT-D structural studies of the energetic material FOX-7. *J Phys Chem C*. 2015;119(5):2322–2334.
104. Zhang J, Xia Y, Zhang Y, et al. Performance improvement of the high resolution neutron diffractometer at CAEP with Geant4 simulation. *J Instrum*. 2017;12, P10007.
105. Doherty RM. *Watt DSJP, Explosives, Pyrotechnics: An International Journal Dealing with Scientific, Materials TAoE. Relationship between RDX properties and sensitivity*. 2008;33(1):4–13.
106. Hoffman D, Martin-Williams A, Gagliardi F, Lorenz T, Willley T, Tran T. *Comparison of DOTC and Legacy Benziger Dry Aminated TATBs and PBX-9502*. Livermore, CA (United States): Lawrence Livermore National Lab.(LLNL); 2013. LLNL-CONF-639860.
107. Wang HF, Xu JJ, Sun SH, et al. Characterization of crystal microstructure based on small angle X-ray scattering (SAXS) technique. *Molecules*. 2020;25(3):443.
108. Yu Q, Zhao CD, Chen JB, et al. Turn a weakness into a strength: performance enhancement of 2,6-Diamino-3,5-dinitropyrazine-1-oxide (LLM-105) via defect engineering. *J Phys Chem C*. 2021;125(4):2739–2747.
109. Xing JT, Wang WL, Dong J, et al. Characterization of the internal pores of LLM-105 with different particle sizes using contrast variation small angle X-ray scattering. *Propellants, Explos Pyrotech*. 2022;47(5), e202100199.
110. Chen B, Dong HS, Dong BZ, et al. Application of SAXS in determination for microstructure of energetic material TATB. *Chinese Journal of atomic and molecular physics*. 2003;20(2):191–196.
111. Xia QZ, Chen B, Zeng GY, et al. Experimental investigation of insensitive explosive C6H6N6O6 by small angle x-ray scattering technique. *Acta Phys Sin-Ch Ed*. 2005;54(7):3273–3277.
112. Yan GY, Huang CQ, Sun GA, Chen B, Huang M, Li HZ. RDX micro-structure by small angle X-ray scattering. *Chin J Energetic Mater*. 2010;18(5):492–496.
113. Tian Q, Yan GY, Sun GA, et al. *Defects Characterization of Molecular Crystal Explosives*. Proceedings of the 2011 International Autumn Seminar on Propellants, Explosives and Pyrotechnics; 2011.
114. Tian Q, Yan GY, Sun GA, et al. Thermally induced damage in hexanitrohexaazaisowurtzitane. *Cent Eur J Energ Mater*. 2013;10(3):359–369.
115. Mark Hoffman D, Willey TM, Mitchell AR, Depiero SC. Comparison of new and legacy TATBs. *J Energetic Mater*. 2008;26(3):139–162.
116. Mang JT, Francois EG, Hagelberg S. Compaction properties of diaminoazoxy furazan (DAAF): a small-angle neutron scattering study. *Int J Energ Mater Chem Propuls*. 2013;12(5):411–428.
117. Mang JT, Hjelm RP. SANS and contrast variation measurement of the different contributions to the total surface area in PBX 9501 as a function of pressing intensity. *AIP Conf Proc*. 2006;845(1):1271–1274.
118. Trevino SF, Wiegand DA. Mechanically induced damage in composite plastic-bonded explosives: a small angle neutron and X-ray study. *J Energetic Mater*. 2008;26(2):79–101.
119. Yan GY, Tian Q, Liu JH, et al. Small-angle X-ray analysis of the effect of grain size on the thermal damage of octahydro-1, 3, 5, 7-tetranitro-1, 3, 5, 7 tetrazocine-based plastic-bounded expolsives. *Chin Phys B*. 2014;23(7), 076101.
120. Willey TM, Overturf G. *Towards Next Generation TATB-Based Explosives by Understanding Voids and Microstructure from 10 Nm to 1 Cm*. Livermore, CA (United States): Lawrence Livermore National Lab. (LLNL); 2009. LLNL-PROC-411719.
121. Ingale SV, Wagh PB, Tewari R, Gupta SC. Nanocrystalline trinitrotoluene (TNT) using sol-gel process. *J Non-Cryst Solids*. 2010;356(41-42):2162–2167.
122. Ingale SV, Sastry PU, Wagh PB, et al. Preparation of nano-structured RDX in a silica xerogel matrix. *Propellants, Explos Pyrotech*. 2013;38(4):515–519.
123. Stepanov V, Willey TM, Ilavsky J, Gelb J, Qiu HW. Structural characterization of RDX-based explosive nanocomposites. *Propellants, Explos Pyrotech*. 2013;38(3):386–393.
124. Yeager JD. *Microstructural Characterization of Simulated Plastic-Bonded Explosives*. Washington State University; 2011.
125. Palmer SJP, Field JE, Huntley JM. Deformation, strengths and strains to failure of polymer bonded explosives. *P Roy Soc Lond a Mat*. 1993;440(1909):399–419.
126. Oswald IDH, Millar DIA, Davidson AJ, et al. High-pressure structural studies of energetic compounds. *High Pres Res*. 2010;30(2):280–291.
127. Fabbiani FPA, Pulham CR. High-pressure studies of pharmaceutical compounds and energetic materials. *Chem Soc Rev*. 2006;35(10):932–942.
128. Choi CS, Boutin HP. A study of the crystal structure of β-cyclotetramethylene tetranitramine by neutron diffraction. *Acta Crystallogr Sect B Struct Crystallogr Cryst Chem*. 1970;26(9):1235–1240.
129. Davidson AJ, Oswald IDH, Francis DJ, et al. Explosives under pressure - the crystal structure of gamma-RDX as determined by high-pressure X-ray and neutron diffraction. *CrystEngComm*. 2008;10(2):162–165.
130. Millar DIA, Oswald IDH, Barry C, et al. Pressure-cooking of explosives-the crystal structure of epsilon-RDX as determined by X-ray and neutron diffraction. *Chem Commun*. 2010;46(31):5662–5664.
131. Baer BJ, Oxley J, Nicol M. The phase diagram of RDX (hexahydro-1, 3, 5-trinitro-s-triazine) under hydrostatic pressure. *High Pres Res*. 1990;2(2):99–108.
132. Ciezak JA, Jenkins TA. The low-temperature high-pressure phase diagram of energetic materials: I. Hexahydro-1,3,5-Trinitro-s-Triazine. *Propellants, Explos Pyrotech*. 2008;33(5):390–395.
133. Millar DIA, Oswald IDH, Francis DJ, Marshall WG, Pulham CR, Cumming AS. The crystal structure of beta-RDX-an elusive form of an explosive revealed. *Chem Commun*. 2009;(5):562–564.
134. Dreger ZA, Gupta YM. Raman spectroscopy of high-pressure-high-temperature polymorph of hexahydro-1,3,5-trinitro-1,3,5-triazine (epsilon-RDX). *J Phys Chem A*. 2010;114(26):7038–7047.
135. Evers J, Klapotke TM, Mayer P, Oehlinger G, Welch J. alpha- and beta-FOX-7, polymorphs of a high energy density material, studied by X-ray single crystal and powder investigations in the temperature range from 200 to 423 K. *Inorg Chem*. 2006;45(13):4996–5007.
136. Crawford MJ, Evers J, Gobel M, et al. gamma-FOX-7: structure of a high energy density material immediately prior to decomposition. *Propellants, Explos Pyrotech*. 2007;32(6):478–495.
137. Pravica M, Liu Y, Robinson J, Velisavljevic N, Liu ZX, Galley M. A high-pressure far- and mid-infrared study of 1,1-diamino-2,2-dinitroethylene. *J Appl Phys*. 2012;111(10), 103534.
138. Konar S, Hunter S, Morrison CA, et al. High-pressure neutron powder diffraction study of epsilon-CL-20: a gentler way to study energetic materials. *J Phys Chem C*. 2020;124(51):27985–27995.
139. Christensen J, Horton PN, Bury CS, et al. Radiation damage in small-molecule crystallography: fact not fiction. *Iucrj*. 2019;6:703–713.
140. Sun J, Kang B, Xue C, et al. Crystal state of 1,3,5-triamino-2,4,6-trinitrobenzene (TATB) undergoing thermal cycling process. *J Energetic Mater*. 2010;28(3):189–201.
141. Cobbledick R, Small R. The crystal structure of the δ-form of 1, 3, 5, 7-tetranitro-1, 3, 5, 7-tetraazacyclooctane (δ-HMX). *Acta Crystallogr Sect B Struct Crystallogr Cryst Chem*. 1974;30(8):1918–1922.
142. Main P, Cobbledick R, Small R. Structure of the fourth form of 1, 3, 5, 7-tetranitro-1, 3, 5, 7-tetraazacyclooctane (γ-HMX), 2C4H8N8O8. 0.5 H2O. *Acta Crystallogr Sect C Cryst Struct Commun*. 1985;41(9):1351–1354.
143. Ghosh M, Banerjee S, Khan MAS, Sikder N, Sikder AK. Understanding metastable phase transformation during crystallization of RDX, HMX and CL-20: experimental and DFT studies. *Phys Chem Chem Phys*. 2016;18(34):23554–23571.
144. Zhang L, Jiang SL, Yu Y, et al. Phase transition in octahydro-1,3,5,7-tetranitro-1,3,5,7-tetrazocine (HMX) under static compression: an application of the first-principles method specialized for CHNO solid explosives. *J Phys Chem B*. 2016;120(44):11510–11522.
145. Rodriguez-Carvajal J, Fernandez-Diaz M, Martinez J. Neutron diffraction study on structural and magnetic properties of La_2NiO_4. *J Phys Condens Matter*. 1991;3(19):3215–3234.
146. Gallagher HG, Miller JC, Sheen DB, Sherwood JN, Vrcelj RM. Mechanical properties of beta-HMX. *Chem Cent J*. 2015;9:22.
147. Ashby MF, Hallam SD. The failure of brittle solids containing small cracks under compressive stress states. *Acta Metall Mater*. 1986;34(3):497–510.
148. Nikolic M, Ibrahimbegovic A, Miscevic P. Brittle and ductile failure of rocks: embedded discontinuity approach for representing mode I and mode II failure mechanisms. *Int J Numer Methods Eng*. 2015;102(8):1507–1526.
149. Li H, Bai LF, Chen XP, et al. Strain-induced structural change and mechanical properties of 1,3,5-triamino-2,4,6-trinitrobenzene probed by neutron diffraction. *Bull Mater Sci*. 2021;44:53.
150. Steele BA, Clarke SM, Kroonblawd MP, et al. Pressure-induced phase transition in 1,3,5-triamino-2,4,6-trinitrobenzene (TATB). *Appl Phys Lett*. 2019;114(19), 191901.
151. Stevens LL, Velisavljevic N, Hooks DE, Dattelbaum DM. Hydrostatic compression curve for triamino-trinitrobenzene determined to 13.0 GPa with powder X-ray diffraction. *Propellants, Explos Pyrotech*. 2008;33(4):286–295.
152. Plisson T, Pineau N, Weck G, Bruneton E, Guignot N, Loubeyre P. Equation of state of 1,3,5-triamino-2,4,6-trinitrobenzene up to 66 GPa. *J Appl Phys*. 2017;122(23), 235901.
153. Liu ZS, Liu DM, Cai YD, Yao YB, Pan ZJ, Zhou YF. Application of nuclear magnetic resonance (NMR) in coalbed methane and shale reservoirs: a review. *Int J Coal Geol*. 2020;218, 103261.
154. Jing S, Sun GA. Analysis of colloidal system structures using spin-echo small-angle neutron scattering. *J Tsinghua Univ*. 2022;62(3):627–632.

Liang-fei Bai received his Ph.D. at the University of Science and Technology of China in 2013. Since then, he has been a member in the Institute of Nuclear Physics and Chemistry, China Academy of Engineering Physics. Currently, he is working as an associate professor and his research interests mainly focus on the development of small-angle scattering techniques and their applications in energetic materials.

Guang-ai Sun received his Ph.D. at the SiChuan University in 2010. He is currently working as a professor in the Institute of Nuclear Physics and Chemistry, China Academy of Engineering Physics. His research interests mainly focus on the development of advanced neutron scattering techniques and their applications in materials science and engineering. E-mail: guangaisun_80@163.com.